Eur. Phys. J. E (2015) **38**: 11
DOI 10.1140/epje/i2015-15011-x

THE EUROPEAN PHYSICAL JOURNAL E

Regular Article

Simulated glass-forming polymer melts: Dynamic scattering functions, chain length effects, and mode-coupling theory analysis

S. Frey[1], F. Weysser[1], H. Meyer[1], J. Farago[1], M. Fuchs[2], and J. Baschnagel[1,a]

[1] Institut Charles Sadron, Université de Strasbourg, CNRS UPR 22, 23 rue du Loess–BP 84047, 67034 Strasbourg Cedex 2, France
[2] Universität Konstanz, Fachbereich Physik, Universitätsstraße 10, 78457 Konstanz, Germany

Received 18 September 2014 and Received in final form 9 January 2015
Published online: 26 February 2015 –

Abstract. We present molecular-dynamics simulations for a fully flexible model of polymer melts with different chain length N ranging from short oligomers ($N = 4$) to values near the entanglement length ($N = 64$). For these systems we explore the structural relaxation of the supercooled melt near the critical temperature T_c of mode-coupling theory (MCT). Coherent and incoherent scattering functions are analyzed in terms of the idealized MCT. For temperatures $T > T_c$ we provide evidence for the space-time factorization property of the β relaxation and for the time-temperature superposition principle (TTSP) of the α relaxation, and we also discuss deviations from these predictions for $T \approx T_c$. For T larger than the smallest temperature where the TTSP holds we perform a quantitative analysis of the dynamics with the asymptotic MCT predictions for the late β regime. Within MCT a key quantity, in addition to T_c, is the exponent parameter λ. For the fully flexible polymer models studied we find that λ is independent of N and has a value ($\lambda = 0.735$) typical of simple glass-forming liquids. On the other hand, the critical temperature increases with chain length toward an asymptotic value T_c^∞. This increase can be described by $T_c^\infty - T_c(N) \sim 1/N$ and may be interpreted in terms of the N dependence of the monomer density ρ, if we assume that the MCT glass transition is ruled by a soft-sphere–like constant coupling parameter $\Gamma_c = \rho_c {T_c}^{-1/4}$, where ρ_c is the monomer density at T_c. In addition, we also estimate T_c from a Hansen-Verlet-like criterion and MCT calculations based on structural input from the simulation. For our polymer model both the Hansen-Verlet criterion and the MCT calculations suggest T_c to decrease with increasing chain length, in contrast to the direct analysis of the simulation data.

1 Introduction

During the past decades the mode-coupling theory (MCT) [1–3] has been among the influential theoretical approaches to the structural glass transition [4,5]. Much of this interest can be explained by the fact that MCT proposes a quantitative description for the onset of the glassy dynamics, which allows to analyze experimental and simulation data [2, 5–7]. A key result of the MCT is the emergence of a two-step decay for all time correlation functions coupling to dynamic (two-point) density fluctuations, when the liquid is cooled from high temperature (T) toward the critical temperature T_c of the theory. This two-step decay is observed in experiment or simulation and arises, according to MCT, from the separation of two relaxation processes: the β process associated with the relaxation of particles inside their neighbor cages and the α process leading to a full renewal of the cage structure and macroscopic flow. For both processes MCT suggests universal results, supposed to be valid for any glass former in the limit $T \to T_c^+$ [1–3]. These results involve for the β process a factorization of the space and time dependence of dynamic scattering functions and for the α process a stretched nonexponential relaxation which obeys the time-temperature superposition principle (TTSP). The range of validity of these universal results has been elaborated by calculating leading-order corrections in terms of the distance to T_c [8,9]. These asymptotic predictions—universal results plus corrections—have provided guidance for tests of the theory by experiment and simulation (see, *e.g.*, refs. [3,6,7] for reviews).

These tests reveal a complex picture. On the one hand, the prediction that the glass transition occurs at T_c is not observed. Instead of diverging, the measured α relaxation time smoothly crosses T_c and continues to grow in a super-Arrhenius fashion. So, T_c is an extrapolated quantity, situated in the regime of the supercooled liquid above the glass transition temperature T_g [3–5]. This shortcoming that

[a] e-mail: jorg.baschnagel@ics-cnrs.unistra.fr

MCT cannot explain the thermal activation of the structural relaxation time was recognized early [2]. Attempts had been made to include "hopping processes" into the theory [1,10], but have raised several concerns [11,12] and were only pursued seldom in the recent past [13]. Finding a predictive theory for the activated dynamics of supercooled liquids remains a major challenge in the research on the glass transition [4,5,14,15]. On the other hand, if one limits the analysis to the temperature regime above T_c, the asymptotic predictions allow for a detailed description of the structural relaxation [3,5–7]. This suggests that the theory captures some important features of the glassy dynamics (which also an extended theory with thermal activation should likely preserve). Moreover, this has stimulated further applications, *e.g.* to systems with competing arrest mechanisms [16–19], and also led to extensions of the theory, *e.g.* to polymer melts [20,21], spatially confined glass-forming liquids [22–25] or colloidal suspensions under shear [26].

In the past years, the asymptotic predictions have also been applied extensively to analyze the slow dynamics in computer simulations of supercooled polymer melts, both for bead-spring models [27–29] and chemically realistic models, like 1,4 polybutadiene [30,31], poly(vinyl methyl ether) [32] or polyisobutylene [33]. These MCT analyses suggest that there are qualitative differences between the limiting cases of a fully flexible bead-spring model and a chemically realistic model. Earlier studies [7,21,34,35] and recent work [27–29] of fully flexible models find values around 0.7 for the exponent parameter λ of the theory. Such values are typical of hard-sphere systems [8,9] or simple glass-forming liquids [6]. Chemically realistic models, however, require larger values near the upper limit $\lambda = 1$ [30–33]. Large λ values are expected within MCT, if different arrest mechanisms simultaneously operate in a system [3,17], for instance, packing constraints and bond formation as in short-ranged attractive colloids [16] or packing constraints and spatial confinement as in statically [36] and dynamically asymmetric binary mixtures [18,19]. For chemically realistic polymer models the different mechanisms could correspond to i) intermolecular packing (as in simple liquids) and ii) intramolecular barriers for conformational transitions [31–33]. Support for this interpretation has come from simulations of bead-spring models, for which the strength of the intramolecular barriers and, along with that, chain stiffness are systematically varied by adding bond-angle and torsional potentials to the fully flexible model [27–29]. These studies indeed find that λ (and T_c) increases with chain stiffness.

In addition to chain stiffness, the length (N) of a chain is another polymer-specific source for slow motion [37,38]. Already for short nonentangled chains it is known that T_g increases with N (see, *e.g.*, [39] and references therein). So, the question arises of whether chain length could also provide a further mechanism for glassy arrest in an MCT analysis. We address this question in the present work. Our study is not the first considering the influence of chain length on the slow dynamics of supercooled, fully flexible bead-spring melts (see, *e.g.*, refs. [40–42]). However, it appears as if a systematic MCT analysis of the interplay of packing and chain-length effects has not been done before. Our analysis shows that chain length does not lead to an additional arrest mechanism in the sense of MCT. We find that λ has a standard value ($\lambda = 0.735$) for all N, while T_c increases with N toward an upper limit. This increase can be explained by packing effects because the monomer density similarly saturates with increasing chain length [42].

Our article is organized as follows. Section 2 describes the model and simulation technique, while sect. 3 provides the necessary theoretical background for the MCT analysis. The results for structural, conformational and dynamic properties are presented in sect. 4. This section also includes a detailed discussion of the fit procedure and of the comparison of the MCT fits with the simulation data. Section 5 summarizes our main findings and puts them into perspective with other work.

2 Model and simulation

2.1 Polymer model

We examine a generic bead-spring model of linear flexible polymer chains, which has been used in previous studies of glass-forming polymer films [43] and of the linear mechanical properties of bulk polymer glasses [39,44]. In this model, the energy of the bond length (l) between consecutive monomers of a chain is given by a harmonic potential

$$U_b(l) = \frac{1}{2} k_b (l - l_0)^2 \tag{1}$$

with the equilibrium bond length $l_0 = 0.967\,\sigma_{LJ}$ and the force constant $k_b = 1110\,\epsilon_{LJ}/\sigma_{LJ}^2$. Here σ_{LJ} and ϵ_{LJ} denote the Lennard-Jones (LJ) diameter of a monomer and the depth of the LJ potential, respectively. Nonbonded monomers of a chain and monomers of different chains interact by a truncated and shifted LJ potential

$$U_{LJ}(r) = \begin{cases} 4\epsilon_{LJ}\left[\left(\frac{\sigma_{LJ}}{r}\right)^{12} - \left(\frac{\sigma_{LJ}}{r}\right)^{6}\right] + C_{LJ}, & \text{for } r < r_{cut}, \\ 0, & \text{else.} \end{cases} \tag{2}$$

The constant $C_{LJ} = 0.02684\,\epsilon_{LJ}$ makes the potential vanish continuously as the distance r between two monomers approaches the cutoff $r_{cut} = 2.3\sigma_{LJ} \simeq 2r_{min}$ with $r_{min} = 2^{1/6}\sigma_{LJ}$ being the minimum of the LJ potential.

In the following all quantities are given in LJ units: temperature (T) in units of ϵ_{LJ}/k_B, distance in units of σ_{LJ}, and time (t) in units of $\tau_{LJ} = (m\sigma_{LJ}^2/\epsilon_{LJ})^{1/2}$, where the monomer mass m and the Boltzmann constant k_B are set to unity.

2.2 Simulation aspects

We carried out molecular-dynamics (MD) simulations of polymer melts having n chains, each with N monomers.

The studied values are $N = 4$ ($n = 3072$), $N = 8$ ($n = 1536$), $N = 16$ ($n = 768$), $N = 32$ ($n = 384$), and $N = 64$ ($n = 192$). The largest chain length is close to the entanglement length of the model [45] and the total number of monomers in the systems is $M = nN = 12288$. All simulations were performed with the LAMMPS code [46] at constant temperature. For simulations at constant volume we used the Nosé-Hoover thermostat with damping parameter $T^{\mathrm{NVT}}_{\mathrm{damp}} = 0.1$ (LAMMPS command `fix nvt`) and for simulations at constant pressure ($P = 0$) the Nosé-Andersen barostat with damping parameters $P^{\mathrm{NPT}}_{\mathrm{damp}} = 75$ and $T^{\mathrm{NPT}}_{\mathrm{damp}} = 10$ (LAMMPS command `fix npt`). Periodic boundary conditions were applied in all spatial directions of the cubic simulation box. The equations of motion were integrated by the velocity Verlet algorithm with a time step of 0.005.

The simulation procedure itself consists of three steps. First, an initial configuration of the polymer melt is set up following ref. [47]. That is, freely rotating chains with (approximately) the correct intrachain statistics but no excluded volume are randomly placed in the simulation box. The size of the simulation box is chosen such that the monomer density is near the target density at the temperature considered (here $T = 1 \gtrsim 2.5T_{\mathrm{g}}$ [43]). Then, the LJ interaction is slowly ramped up to its full value. In the second step, the melt is equilibrated at $T = 1$ while imposing $P = 0$. This allows the system to find its equilibrium volume. As a criterion for equilibration we require that the correlation function of the end-to-end vector ($\boldsymbol{R}_{\mathrm{e}}$), $\varphi_{\mathrm{e}}(t) = \langle \boldsymbol{R}_{\mathrm{e}}(t) \cdot \boldsymbol{R}_{\mathrm{e}}(0)\rangle / \langle \boldsymbol{R}^2_{\mathrm{e}}(0)\rangle$, attains a value of 0.1. This criterion is sufficient, since $\varphi_{\mathrm{e}}(t)$ probes the slowest relaxation of the melt [37, 38]. Starting from the equilibrated configuration at $T = 1$ the system is continuously cooled down to $T = 0.5$ with a cooling rate of $\Gamma_T = 10^{-5}$. At $T = 0.5$ nonequilibrium effects due to the finite cooling rate are very weak and can be eliminated quickly by isothermal equilibration (at $P = 0$). Lower temperatures are then reached by reducing T in a stepwise fashion by $\Delta T = 0.01$, always followed by an equilibration run until $\varphi_{\mathrm{e}}(t) \leq 0.1$. Finally, in the third step we determine the average volume for each equilibrated configuration and perform canonical simulations at the resulting volume (only Nosé-Hoover thermostat), yielding the time series used for the analyses in this work.

3 Theoretical background

We analyze our simulation results in the framework of the idealized mode-coupling theory [3, 8, 9]. MCT predicts a bifurcation scenario for the coherent scattering function,

$$\phi_q(t) = \frac{1}{MS(q)} \sum_{i,j=1}^{M} \langle \exp\{\mathrm{i}\boldsymbol{q} \cdot [\boldsymbol{r}_i(t) - \boldsymbol{r}_j(0)]\}\rangle \,, \qquad (3)$$

and for all quantities coupling to collective density fluctuations, *e.g.* also for the incoherent scattering function,

$$\phi^{\mathrm{s}}_q(t) = \frac{1}{M} \sum_{i=1}^{M} \langle \exp\{\mathrm{i}\boldsymbol{q} \cdot [\boldsymbol{r}_i(t) - \boldsymbol{r}_i(0)]\}\rangle \,. \qquad (4)$$

Here q denotes the absolute value of the wave vector $\boldsymbol{q}$, $\boldsymbol{r}_i(t)$ is the position of monomer i at time t and $S(q)$ is the static structure factor (see eq. (18)). $\phi_q(t)$ and $\phi^{\mathrm{s}}_q(t)$ are real-valued and depend on $\boldsymbol{q}$ only through its scalar invariant q, as the polymer liquid is isotropic and translationally invariant. The bifurcation scenario of MCT then implies that there is a critical temperature (T_{c}) where the nonergodicity parameters f_q, f^{s}_q,

$$f_q(T) = \lim_{t\to\infty} \phi_q(t) \quad \text{and} \quad f^{\mathrm{s}}_q(T) = \lim_{t\to\infty} \phi^{\mathrm{s}}_q(t), \qquad (5)$$

jump discontinuously from zero for $T > T_{\mathrm{c}}$ to finite values $f_q(T_{\mathrm{c}}) = f^{\mathrm{c}}_q$ and $f^{\mathrm{s}}_q(T_{\mathrm{c}}) = f^{\mathrm{sc}}_q$. It is therefore interesting to analyze the theory on the relative temperature scale $\varepsilon = (T_{\mathrm{c}} - T)/T_{\mathrm{c}}$. To quantify the distance to the critical point MCT introduces the separation parameter σ which is proportional to ε,

$$\sigma = C\varepsilon \quad (C = \text{system-specific constant}), \qquad (6)$$

provided T is close to T_{c}. The following equations are predictions in leading order of $|\sigma|$.

The separation parameter determines the temperature dependence of two time scales: the β-relaxation time t_σ

$$t_\sigma = \frac{t_0}{|\sigma|^{1/2a}} \quad (0 < a < 0.3953) \qquad (7)$$

and the α-relaxation time t'_σ

$$t'_\sigma = \frac{t_0}{|\sigma|^{\gamma}} \,, \quad \gamma = \frac{1}{2a} + \frac{1}{2b} \quad (\gamma > 1.765). \qquad (8)$$

Equation (7) holds for $T \to T^{\pm}_{\mathrm{c}}$, eq. (8) only for $T \geq T_{\mathrm{c}}$. In both equations t_0 denotes a system-specific microscopic time. The exponents a and b are called respectively critical exponent and von Schweidler exponent. They are related to each other by the "exponent parameter" λ,

$$\lambda = \frac{\Gamma(1-a)^2}{\Gamma(1-2a)} = \frac{\Gamma(1+b)^2}{\Gamma(1+2b)} \,, \qquad (9)$$

where Γ is the Gamma function.

Equations (7) and (8) indicate that t'_σ diverges more strongly than t_σ on cooling toward T_{c}. Due to this separation of the time scales MCT predicts a two-step relaxation scenario. The first step encompasses times on the scale t_σ (*i.e.* $t_0 \ll t \ll t'_\sigma$) for which the correlators $\phi_q(t)$ and $\phi^{\mathrm{s}}_q(t)$ remain close to their nonergodicity parameters, *i.e.*, for which $|\phi_q(t) - f^{\mathrm{c}}_q| \ll 1$ and $|\phi^{\mathrm{s}}_q(t) - f^{\mathrm{sc}}_q| \ll 1$. This time regime is called β process (or β-relaxation regime). The second step corresponds to the α process (or α-relaxation regime) where the correlators decay from the nonergodicity parameter to zero for times on the scale t'_σ.

In the β-relaxation regime MCT predicts a factorization theorem for $\phi_q(t)$ and $\phi^{\mathrm{s}}_q(t)$. The theorem states that the wave-vector and time dependent correction to the nonergodicity parameter factorizes so that the scattering functions may be written as

$$\begin{aligned} \phi_q(t) &= f^{\mathrm{c}}_q + h_q G(t), \\ \phi^{\mathrm{s}}_q(t) &= f^{\mathrm{sc}}_q + h^{\mathrm{s}}_q G(t). \end{aligned} \qquad (10)$$

The critical amplitudes h_q, $h_q^{\rm s}$ are independent of temperature (near $T_{\rm c}$). The temperature dependence only enters by the β correlator $G(t)$. On approach to $T_{\rm c}$ from above this T dependence is given by

$$G(t) = \sqrt{|\sigma|}g(t/t_\sigma) \xrightarrow{t\gg t_\sigma} -B\sqrt{|\sigma|}\left(\frac{t}{t_\sigma}\right)^b = -B\left(\frac{t}{t'_\sigma}\right)^b. \qquad (11)$$

Here $B = B(\lambda)$ is a constant [48] and $G(t) \sim -(t/t'_\sigma)^b$ is called von Schweidler law which holds for $t_\sigma \ll t \ll t'_\sigma$. The factorization theorem and the von Schweidler law are MCT results in leading order of $|\sigma|$. Corrections have been worked out [3,8,9]. For long times ($t \gg t_\sigma$) they take the following form:

$$\phi_q(t) = f_q^{\rm c} - h_q B\left(\frac{t}{t'_\sigma}\right)^b + h_q B^2 B_q\left(\frac{t}{t'_\sigma}\right)^{2b}, \qquad (12)$$

$$\phi_q^{\rm s}(t) = f_q^{\rm sc} - h_q^{\rm s} B\left(\frac{t}{t'_\sigma}\right)^b + h_q^{\rm s} B^2 B_q^{\rm s}\left(\frac{t}{t'_\sigma}\right)^{2b}. \qquad (13)$$

These corrections violate the factorization theorem due to the q dependence of B_q, $B_q^{\rm s}$. Near $T_{\rm c}$ the amplitudes B_q and $B_q^{\rm s}$ may be taken as independent of temperature (in the same way as h_q, $h_q^{\rm s}$). The analysis of our simulation data in the β regime is based on eqs. (12) and (13).

The α-relaxation regime deals with the dynamics for times $t \sim t'_\sigma$. Here MCT predicts that the scattering functions are described by the T independent α master curves (for $\sigma \to 0^-$):

$$\phi_q(t) = \tilde{\phi}_q(t/t'_\sigma), \qquad \phi_q^{\rm s}(t) = \tilde{\phi}_q^{\rm s}(t/t'_\sigma), \qquad (14)$$

which have the following limits for $t \to 0$,

$$\tilde{\phi}_q(t\to 0) = f_q^{\rm c} \quad \text{and} \quad \tilde{\phi}_q^{\rm s}(t\to 0) = f_q^{\rm sc}, \qquad (15)$$

and give back the von Schweidler law (11) for $t \ll t'_\sigma$. Therefore, the α and β relaxations overlap for times $t_\sigma \ll t \ll t'_\sigma$. Equation (14) implies that the α process obeys the time-temperature superposition principle (TTSP): Correlators for different T collapse onto the same master curve when rescaled by some relaxation time that is proportional to t'_σ. In particular, if we choose the relaxation time τ_q as a time in the α regime, defined by $\phi_q(\tau_q) = \text{const}$, we have

$$\tau_q = C_q t'_\sigma, \qquad (16)$$

with C_q being a T independent constant which contains the q dependent part of the relaxation time. This prediction will be tested for our simulation data.

4 Results

4.1 Static properties

Figure 1 depicts the monomer density (ρ) for all temperatures and chain lengths. Over the T range studied we

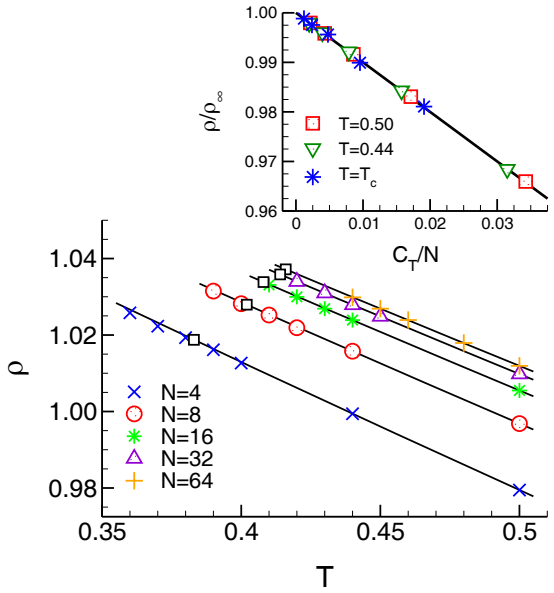

Fig. 1. Main panel: Monomer density ρ *versus* T for different N (symbols). The solid lines represent a parameterization of the data by $\rho(T,N) = \rho(0.5,N)\exp[-\alpha_N(T-0.5)]$, where $\rho(0.5,N)$ is the monomer density of the melt with chain length N at $T = 0.5$ and α_N its thermal expansion coefficient. With $\rho(0.5,4) = 0.9795$, $\rho(0.5,8) = 0.9968$, $\rho(0.5,16) = 1.0055$, $\rho(0.5,32) = 1.0098$ and $\rho(0.5,64) = 1.0119$ the fits yield $\alpha_4 = 0.3360$, $\alpha_8 = 0.3134$, $\alpha_{16} = 0.3022$, $\alpha_{32} = 0.2961$ and $\alpha_{64} = 0.2933$. The parameterization allows to interpolate or extrapolate the data to determine the monomer density $\rho_{\rm c}$ at $T_{\rm c}$ (table 1); $\rho_{\rm c}$ is indicated by an open square. Inset: Monomer density as a function of N for $T = 0.5$, 0.44 and $T_{\rm c}$. The data are scaled according to eq. (17) with the fit parameters: $\rho_\infty(0.5) = 1.014$, $C_{0.5} = 0.137$; $\rho_\infty(0.44) = 1.032$, $C_{0.44} = 0.126$; $\rho_\infty(T_{\rm c}) = 1.038$, $C_{T_{\rm c}} = 0.076$.

may assume that the thermal expansion coefficient α_N ($= -\partial \ln\rho/\partial T$) of the polymer liquid is constant [39,43]. Thus, the density-temperature trace can be parameterized by $\rho(T,N) = \rho(0.5,N)\exp[-\alpha_N(T-0.5)]$ (solid lines in fig. 1). This parameterization allows interpolations or extrapolations to determine pairs of temperatures and densities which were not simulated, as for example the critical density $\rho_{\rm c}$ corresponding to the critical temperature $T_{\rm c}$ found from the MD simulations (open squares in fig. 1).

For fixed temperature fig. 1 shows that the density increases with N toward an asymptote $\rho_\infty(T)$. Since the work by Fox and Flory (see, *e.g.*, [49] and references therein) this N dependence is usually interpreted as a chain-end effect, associating an extra free volume ($V_{\rm e}$) with the chain ends compared to inner monomers. This argument yields the following relation:

$$\rho(T,N) = \frac{\rho_\infty(T)}{1+\rho_\infty V_{\rm e}/N} \simeq \rho_\infty(T)\left(1 - \frac{C_T}{N}\right), \qquad (17)$$

where the last equality holds, if the constant C_T ($= \rho_\infty V_{\rm e}$) is small. For flexible bead-spring models (as ours) C_T is expected to be small [41] because the efficient packing of the monomers limits the extra volume of the chain ends, which

is caused by the fact that end monomers, having only one binding partner, occupy more space. Equation (17) then implies that all (T, ρ) pairs should collapse onto a master curve when scaled by ρ_∞ and C_T/N. This is demonstrated in the inset of fig. 1 for two selected temperatures. Furthermore, the inset shows that the relation (17) also holds for the monomer density ρ_c evaluated at the critical temperature $T_c(N)$.

In addition to the average density static density fluctuations are key properties of glass-forming liquids. They can be characterized by the collective static structure factor $S(q)$,

$$S(q) = \frac{1}{M} \sum_{i,j=1}^{M} \langle \exp\left[\mathrm{i}\boldsymbol{q} \cdot (\boldsymbol{r}_i - \boldsymbol{r}_j)\right] \rangle \,, \tag{18}$$

and the direct correlation function $c(q)$ that is defined by the generalized Ornstein-Zernike equation via [50,51]

$$\rho c(q) = \frac{1}{w(q)} - \frac{1}{S(q)} = \frac{\rho h(q)}{w(q) S(q)} \,, \tag{19}$$

where

$$w(q) = \frac{1}{N} \sum_{i,j=1}^{N} \langle \exp\left[\mathrm{i}\boldsymbol{q} \cdot (\boldsymbol{r}_i - \boldsymbol{r}_j)\right] \rangle \tag{20}$$

denotes the intrachain structure factor (the form factor of a polymer) and

$$h(q) = \left[S(q) - w(q)\right] / \rho \tag{21}$$

is the intermolecular pair-correlation function [50].

Figure 2 shows $S(q)$ for $N = 4$ and $T = 0.36$, 0.38, 0.44, 0.7 ($T_c = 0.383$, cf. table 1). In this T range the shape of $S(q)$ is characteristic of a liquid (see, *e.g.*, [28,52] or [7] and references therein). For $q \to 0$ the structure factor is small due to the low compressibility of the melt. For larger wave vectors $S(q)$ displays oscillations around 1. The amplitude of these oscillations quickly decreases with increasing q. So, no long-range structural correlations develop; the system stays amorphous for all T shown. The strongest temperature dependence is found near the first peak of $S(q)$, occurring at $q^* \approx 7$, which indicates the average monomer separation and roughly corresponds to the length scale of the monomer diameter. With decreasing T the peak position and the peak height shift to larger values. This reflects the increase of the density and the attendant tighter nearest-neighbor packing on cooling [28,52]. Similar behavior is found for all chain lengths.

Within MCT the slowdown of the dynamics is mainly driven by the local cage effect, *i.e.*, by wave vectors near q^* [3,20,21]. It is therefore expected that an estimate of T_c can be obtained by an extension of the (empirical) Hansen-Verlet freezing criterion [53] to glass-forming liquids. This criterion states that a liquid transitions to a solid when $S(q^*)$ reaches a certain threshold. Ideal MCT suggests $S(q^*) = 3.54$ at the liquid-glass transition for hard spheres [54]. We apply this criterion here. The inset of fig. 2 depicts the T dependence of $S(q^*)$ for $N = 4$, 16, and 64. Whereas for $N \leq 16$ we have equilibrated configurations below and above $S(q^*) = 3.54$ so that T_c can be determined by an interpolation, an extrapolation from high T is required for $N \geq 32$. Of course, such an extrapolation introduces uncertainties. Nevertheless, we find that the qualitative trend for the interpolated and extrapolated critical temperatures is the same: The Hansen-

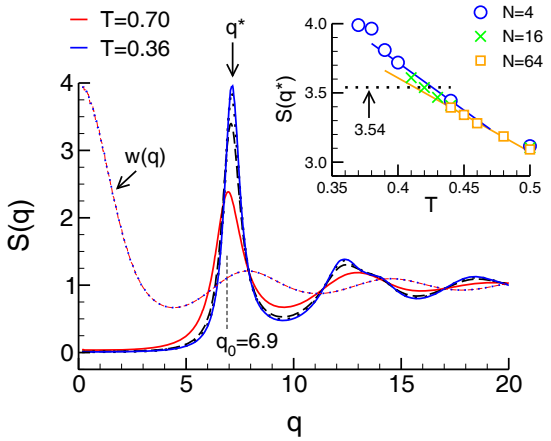

Fig. 2. Main panel: Static structure factor $S(q)$ for $N = 4$ and $T = 0.36$, 0.38, 0.44, 0.7 ($T_c = 0.383$). The (T dependent) position of the first maximum (q^*) and a fixed wave vector close to q^* ($q_0 = 6.9$) are indicated. The thin dashed and dotted lines show the form factor $w(q)$ for $T = 0.7$ and $T = 0.36$, respectively. Inset: $S(q)$ at q^* *versus* T for different N ($6.96 \lesssim q^* \lesssim 7.16$ for the temperatures shown). The horizontal dotted line shows the Hansen-Verlet criterion for the glass transition of hard spheres within the ideal MCT ($S(q^*) = 3.54$) [54]. The solid line for $N = 4$ is an interpolation between the two data points above and below $S(q^*) = 3.54$; for $N = 64$ the solid line is an extrapolation using the two lowest T.

Table 1. Survey of MCT parameters. $T_{c,HV}$ is the critical temperature estimated from $S(q)$ via the Hansen-Verlet criterion (fig. 2). Results from an MCT calculation based on static input (sect. 4.3.2) are denoted by the subscript "MCT". As for $T_{c,HV}$, the critical temperature $T_{c,MCT}$ decreases with increasing N. On the other hand, the exponent parameter λ_{MCT} (eq. (9)) and the associated exponents a_{MCT}, b_{MCT} and γ_{MCT} (eq. (8)) can be taken as independent of N. For the exponent parameter and the associated exponents the MCT calculation gives values that agree well with the fit results using the asymptotic predictions (sect. 4.3.1). These fit results are denoted by λ, a, b and γ; they can also be taken as independent of N. However, the critical temperature T_c from the fits depends on chain length; it increases with N. The corresponding monomer density $\rho_c = \rho(T_c)$ is taken from fig. 1. ($a = 0.312$, $b = 0.582$, $\gamma = 2.464$, $\lambda = 0.735$, $B = 0.837$, $a_{MCT} = 0.317$, $b_{MCT} = 0.602$, $\gamma_{MCT} = 2.408$, $\lambda_{MCT} = 0.723$.)

N	4	8	16	32	64
$T_{c,HV}$	0.426	0.422	0.420	0.416	0.413
$T_{c,MCT}$	0.322	0.275	0.247	0.229	0.221
T_c	0.383	0.402	0.408	0.414	0.416
ρ_c	1.0187	1.0279	1.0339	1.0358	1.0372

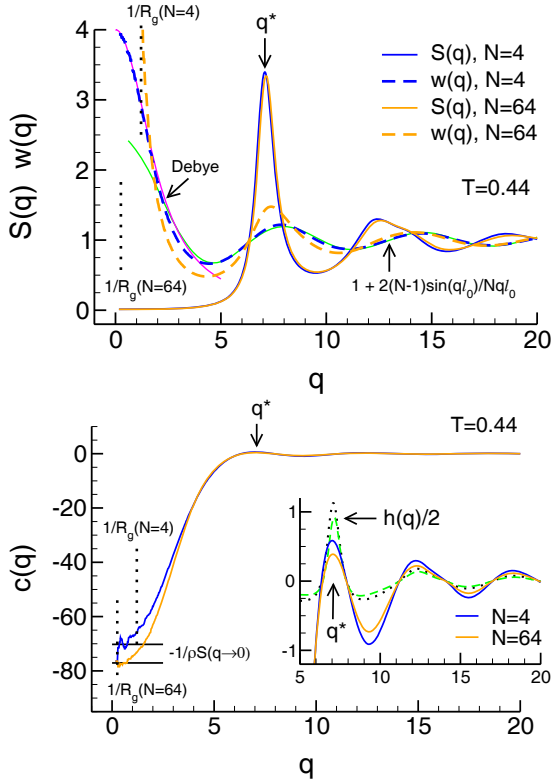

Fig. 3. Upper panel: $S(q)$ (solid lines) and $w(q)$ (dashed lines) for $N = 4$ and $N = 64$ at $T = 0.44$ ($T_c(N = 4) = 0.383$, $T_c(N = 64) = 0.416$). The position q^* (≈ 7.09) of the first peak of $S(q)$ is indicated. The vertical dotted lines depict the q values where $q = 1/R_g$ for both chain lengths ($R_g(N = 4) = 0.824$, $R_g(N = 64) = 3.923$). For $w(q)$ two theoretical curves are shown by thin solid lines, the Debye curve (23) and the large-q approximation (22). Lower panel: Direct correlation function $c(q)$ for $N = 4$ and $N = 64$ at $T = 0.44$ (eq. (19)). The modulus of the wave vectors for q^* and $1/R_g$ are indicated as in the upper panel. The horizontal lines show $-1/\rho S(q \to 0)$ ($S(q \to 0) \simeq 0.0143$ for $N = 4$, $S(q \to 0) \simeq 0.0126$ for $N = 64$). The inset magnifies the behavior of $c(q)$ for $q \gtrsim q^*$ and also compares $c(q)$ with the intermolecular pair-correlation function $h(q)$ for both N (dotted line for $N = 4$, dashed line for $N = 64$). To put $h(q)$ on the scale of the figure $h(q)/2$ is shown.

Verlet criterion suggests that T_c decreases with increasing N (denoted by $T_{c,HV}$ in table 1). We will compare this suggestion with the results from the quantitative analysis with the asymptotic MCT predictions in sect. 4.3.

The upper panel of fig. 3 compares $S(q)$ and $w(q)$ for two chain lengths, $N = 4$ and 64, at $T = 0.44$. For the form factor we can distinguish two regimes. If $q \to \infty$, $w(q)$ probes the smallest distance (l_0) along the chain. Following ref. [51] we expect that $w(q)$ is given by

$$w(q) \approx 1 + \frac{2(N-1)}{N} \frac{\sin(ql_0)}{ql_0} \quad (q \text{ large}). \qquad (22)$$

Figure 3 shows that this approximation agrees well with the MD data for $q \gtrsim 10$ and explains the weak chain-length dependence of $w(q)$ for large q. The dependence on N is much stronger in the opposite limit $q \to 0$, where $w(q)$ reflects the chain size and behaves as $w(q \to 0) = N(1 - q^2 R_g^2/3)$ with R_g being the radius of the gyration of a chain [37,38]. Since (long) flexible polymers in melts have approximately [55] an ideal random-walk–like structure on intermediate and large length scales, the Debye function,

$$w_D(q) = N f_D(q^2 R_g^2), \qquad f_D(x) = \frac{2}{x^2}\left(e^{-x} + x - 1\right), \qquad (23)$$

is commonly used to describe $w(q)$ for $q \ll 1/l_0$ [37,38]. For $q < 1/R_g$ the form factor from the simulation and the Debye function must agree, irrespective of chain length, because $w(q \to 0) = w_D(q \to 0)$ (cf. fig. 3). For $1/R_g < q < 1/l_0$, however, deviations from eq. (23) are expected, not only for short chains (as ours) where the length scales l_0 and R_g are not well separated, but also for long chains due to corrections to chain ideality [55]. In addition to the temperature dependence of R_g, the latter corrections introduce an extra T dependence via the density. However, both ρ and R_g depend only weakly on T for our model. Therefore, the fact that $w(q)$ is (almost) independent of temperature can be understood (see fig. 2) [51]. A negligible T dependence of $w(q)$ is also observed in other simulations of flexible bead-spring models [28]. A stronger T dependence is found for stiffer chain models with bond-angle and torsional potentials which affect in particular the small-q behavior due to an increase of R_g on cooling. However, the overall T dependence is reported to be weak compared to that of $S(q)$ [28].

From fig. 3 we also see that $S(q)$ has a much weaker dependence on chain length than $w(q)$. This means that the intermolecular pair-correlation function $h(q)$ nearly compensates the N dependence of $w(q)$ (eq. (21)). For small wave vectors we have $S(q \to 0) \approx 10^{-2}$ and so $\rho h(q) \approx -w(q)$. This "correlation hole effect" [50,56] implies that the direct correlation function $c(q)$ is determined by the inverse compressibility of the melt (eq. (19)). From the lower panel of fig. 3 we see that $|c(q \to 0)|$ increases with N. According to MCT, however, this N dependence is not crucial because the glass transition is driven by wave vectors near the first peak of $S(q)$ [8]. For $q \sim q^*$ we find that $S(q)$ slightly decreases with N, while $w(q)$ increases with N. Thus, $h(q)$ is smaller for $N = 64$ than for $N = 4$, and this impacts $c(q)$ (eq. (19)). Figure 3 shows that $c(q)$ closely traces the dependence of $h(q)$ on N for $q \gtrsim q^*$. Therefore, the effective monomer-monomer interaction becomes weaker as N increases. This suggests that an MCT calculation based on this structural input (as done in [21,28,29]) would predict T_c to decrease with increasing N, in agreement with the Hansen-Verlet criterion. We test this suggestion for our model (see sects. 4.3.2 and 4.3.3).

4.2 MCT analysis: Qualitative features

We turn now to an MCT analysis of the dynamics. The analysis begins with qualitative tests of the two main predictions in the β regime (factorization theorem, eq. (10))

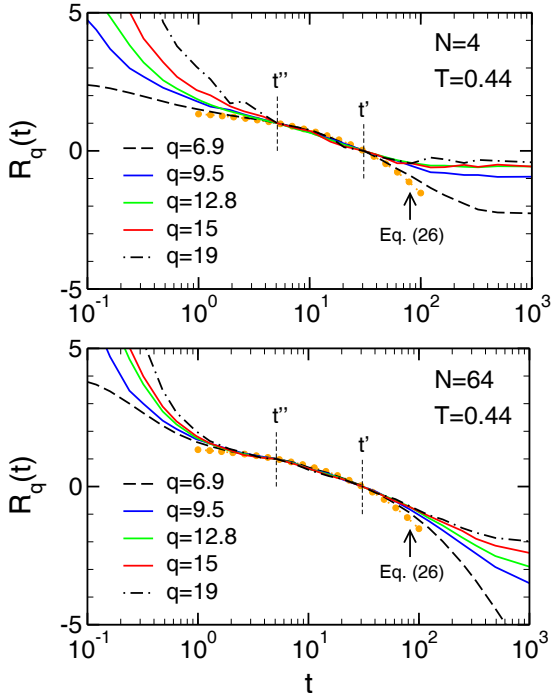

Fig. 4. Test of the factorization theorem for $\phi_q(t)$ and $q \geq q_0 = 6.9$ via eq. (24). Upper panel: $N = 4$, $T = 0.44$ ($T_c = 0.383$). Lower panel: $N = 64$, $T = 0.44$ ($T_c = 0.416$). By definition, $R_q(t'' = 5.12) = 1$ and $R_q(t' = 30.72) = 0$. The times t' and t'' are indicated by vertical dashed lines. In both panels the filled (orange) circles show eq. (26) with b taken from table 1.

and α regime (TTSP, eq. (14)). Not only shall these tests reveal whether an application of MCT can be promising at all (not every two-step relaxation needs to be related to the physics described by MCT [30,57]), they also inform on the range of validity of the ideal theory, which guides the further quantitative analysis (see sect. 4.3.1).

The factorization theorem can be tested by fixing two times t'' and t' ($> t''$) in the β regime and evaluating the following relations:

$$R_q(t) = \frac{\phi_q(t) - \phi_q(t')}{\phi_q(t'') - \phi_q(t')} = \frac{G(t) - G(t')}{G(t'') - G(t')} \qquad (24)$$

$$= \frac{\phi_q^{\rm s}(t) - \phi_q^{\rm s}(t')}{\phi_q^{\rm s}(t'') - \phi_q^{\rm s}(t')} = R_q^{\rm s}(t), \qquad (25)$$

where $G(t)$ is the β correlator (eq. (10)). These equations show that $R_q(t)$, $R_q^{\rm s}(t)$ are independent of q. Thus, superimposing $R_q(t)$ and $R_q^{\rm s}(t)$ for different q should result in a collapse over a time window where the β scaling holds. The advantage of this method is that it works directly with the simulation (or experimental) data. Consequently, this test is easy to implement and has been widely applied in simulations of simple glass formers [52, 58–61], silica glasses [62,63] and polymeric glass formers [28,31–33,35].

As demonstrated in fig. 4 such a collapse is indeed possible. The upper panel depicts $R_q(t)$ for $N = 4$ at $T = 0.44$ for various q values near the maxima and minima of $S(q)$. The lower panel shows $R_q(t)$ for $N = 64$ at $T = 0.44$ for the same q values. For $N = 64$ the factorization theorem holds over almost one and a half decades, whereas for $N = 4$ the region of collapse hardly spans a decade. This can be explained by the fact that the $N = 4$ system is farther away from T_c ($\varepsilon = -0.1488$) than the $N = 64$ system ($\varepsilon = -0.05767$). Here T_c refers to the critical temperature as obtained from the analysis of sect. 4.3.3 (cf. table 1). In fact, for relative distances $-0.1 \lesssim \varepsilon \lesssim -0.05$ one should not expect the leading-order result (10) to hold over more than one decade in time [8]. By combining eqs. (10) and (11) we get a simple expression for $R_q(t)$ and $R_q^{\rm s}(t)$,

$$R_q(t) = R_q^{\rm s}(t) = \frac{t^b - t'^b}{t''^b - t'^b}\,. \qquad (26)$$

With the result $b = 0.582$ from sect. 4.3.3 (cf. table 1) the circles in fig. 4 show that eq. (26) gives a good description of the MD data in the time regime where the data collapse is observed.

Figure 4 also shows that the data splay out at early and late times. This splaying out is q-dependent and can serve as a further sensitive test of the MCT asymptotics. In the β regime MCT predicts an ordering rule [8,9]: Since in the next-to-leading order corrections to the factorization theorem the same q dependent amplitudes appear both for the early-time and long-time corrections, correlators that lie, for example, above the factorization theorem for short times must also lie above it for long times. Thus, when numbering the correlators in the order in which they enter the collapse regime, this numbering should be preserved when the correlators leave the regime [8]. Figure 4 confirms this prediction for our model. This has also been observed in many other simulations [28,31–33,52,59,61].

Figure 5 extends the analysis to $T \simeq T_c$, *i.e.*, to the T regime where additional relaxation channels, not accounted for by MCT, compromise the ideal glass transition scenario [11–14]. Nevertheless, we find that the data still collapse in an intermediate time window onto a master curve which is the same for both $R_q(t)$ and $R_q^{\rm s}(t)$ (the latter result also holds for $T > T_c$.) Therefore, even for $T \simeq T_c$ the coherent and incoherent correlators continue to display a factorization property into a t-dependent and q-dependent contribution. However, the ideal MCT can no longer rationalize the features observed in fig. 5. For instance, we see that the ordering rule is violated. Furthermore, ideal MCT would have expected the liquid to vitrify at T_c, but the master curve is still described by eq. (26) with the same exponent b as found above T_c. The latter observation, *i.e.* that eqs. (12), (13) with the same b as above T_c can be applied for $T \lesssim T_c$, was also made in other simulations [30,32].

We turn now to a test of the TTSP for the α relaxation. According to eqs. (14) and (16) plotting the correlation functions as a function of rescaled time t/τ_{q_0} should allow to superimpose the data for long times onto a master curve as $T \to T_c^+$. We determine the scaling time τ_{q_0} with $q_0 = 6.9$ by the condition $\phi_{q_0}(\tau_{q_0}) = 0.1$. This threshold value is arbitrary, yet fulfills two criteria: It is small enough for the correlator to be definitely in the α regime and large enough to be above the noise level. Note that $q_0 = 6.9$ is

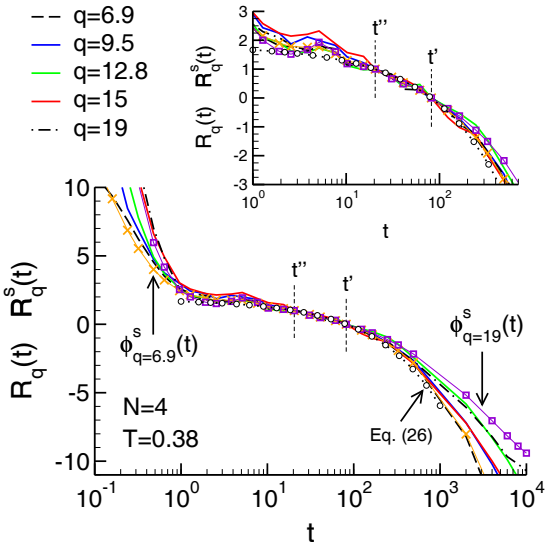

Fig. 5. Test of the factorization theorem for $N = 4$ and $T = 0.38$ ($\simeq T_c$) by eqs. (24) and (25). The lines show $\phi_q(t)$ for $q \geq q_0$. The symbols depict $\phi_q^s(t)$ for two wave vectors (crosses for $q_0 = 6.9$, squares for $q = 19$). By definition, $R_q(t'' = 20.48) = R_q^s(t'' = 20.48) = 1$ and $R_q(t' = 81.92) = R_q^s(t' = 81.92) = 0$. The times t' and t'' are indicated by vertical dashed lines. The inset shows a zoom of $R_q(t)$ and $R_q^s(t)$ for times close to t' and t''. In the main figure and the inset the open circles (connected by a dotted line) show $R_q(t)$, $R_q^s(t)$ evaluated from eq. (26) with b taken from table 1.

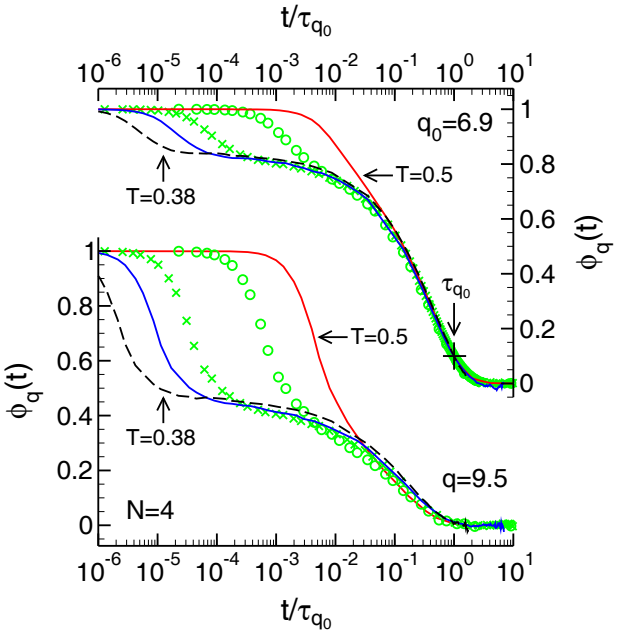

Fig. 6. Test of the TTSP for $N = 4$: $\phi_q(t)$ as a function of t/τ_{q_0} for $q = q_0 = 6.9$ (upper figure) and $q = 9.5$ (lower figure). Five temperatures are shown (from left to right): $T = 0.38$ ($\simeq T_c$), 0.39, 0.4, 0.44, and 0.5. The definition of the scaling time τ_{q_0} by the condition $\phi_{q_0}(\tau_{q_0}) = 0.1$ is indicated by a cross in the upper figure. For $q = 6.9$ the TTSP extends to shorter rescaled times with decreasing temperature for $T \geq 0.4$. For $T \leq 0.39$ the scaling is violated. For $q = 9.5$ and $T \geq 0.4$ time-temperature superposition with τ_{q_0} works less well than for q_0.

close to the position of the main peak of $S(q)$, where the strength of the α process is most pronounced and the best separation from the β regime can be achieved.

The upper panel of fig. 6 depicts the rescaling for $\phi_q(t)$ at $q = 6.9$ for $N = 4$ and $T = 0.38$, 0.39, 0.4, 0.44, 0.5 ($T_c = 0.383$). The TTSP is fulfilled for all T above 0.39, but becomes violated for smaller temperatures. For $T = 0.38$ deviations are clearly visible: The plateau value is increased, making $\phi_q(t)$ to lie above the master curve obtained for higher T. Such deviations from the ideal MCT must occur because $T = 0.38 \lesssim T_c$ where the theory would expect the system to be in the glass phase [3,8]. Contrary to that, $\phi_q(t)$ exhibits a relaxation to zero. Similar behavior is also found for other wave vectors. The lower panel of fig. 6 gives an example by showing $\phi_q(t)$ for $q = 9.5$ (first minimum of $S(q)$) with time rescaled by τ_{q_0}. Quite generally, we see that the scaling is worse than for q_0. A similar superposition as for q_0 could have been obtained, had time be rescaled by $\tau_{q=9.5}$ instead of by τ_{q_0}. This illustrates that the α-relaxation times at different wave numbers have somewhat different T dependence, in contrast to eq. (16), but as observed in many simulation studies (see, *e.g.*, [7,52,60,64,65]).

Figure 7 extends the test of the TTSP to $N = 64$. The scaling time τ_{q_0} is again determined by the condition $\phi_{q_0}(\tau_{q_0}) = 0.1$. We obtain results similar to those of the $N = 4$ system. The TTSP works better for q_0 than for $q = 9.5$ and is well fulfilled for all T shown because the temperatures are larger than T_c ($= 0.416$).

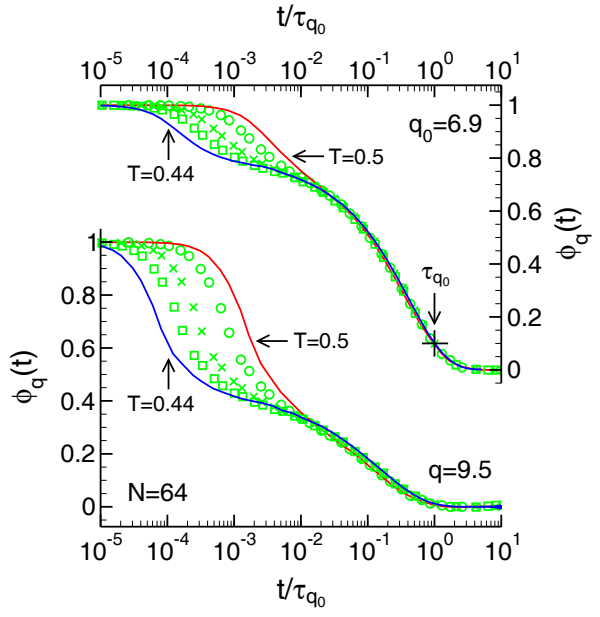

Fig. 7. Test of the TTSP for $N = 64$: $\phi_q(t)$ as a function of t/τ_{q_0} for $q = q_0 = 6.9$ (upper figure) and $q = 9.5$ (lower figure). Five temperatures are shown (from left to right): $T = 0.44$, 0.45, 0.46, 0.48, and 0.5 ($T_c = 0.416$). The definition of the scaling time τ_{q_0} by the condition $\phi_{q_0}(\tau_{q_0}) = 0.1$ is indicated by a cross in the upper figure. For all T shown the TTSP extends to shorter rescaled times with decreasing temperature. For $q = 9.5$ the scaling with τ_{q_0} is worse than for q_0.

4.3 Quantitative MCT analysis

4.3.1 Description of the fit procedure using the asymptotic MCT predictions

The quantitative analysis of the slow dynamics in the supercooled state is based on the MCT prediction for the late-β regime ($t \gg t_\sigma$)

$$\phi_q(t) = f_q^{\rm c} - h_q^{\rm fit}\left(\frac{t}{t'_\sigma}\right)^b + h_q^{\rm fit}B_q^{\rm fit}\left(\frac{t}{t'_\sigma}\right)^{2b} \qquad (27)$$

with the fit constants $h_q^{\rm fit}$, $B_q^{\rm fit}$ being connected to h_q, B_q (eq. (12)) as

$$h_q^{\rm fit} = h_q B \quad \text{and} \quad B_q^{\rm fit} = BB_q. \qquad (28)$$

The same equations also hold for the incoherent scattering with the substitutions $f_q^{\rm c} \to f_q^{\rm sc}$, $h_q \to h_q^{\rm s}$, and $B_q \to B_q^{\rm s}$ (eq. (13)).

The fit must furnish five parameters, four of which are independent of temperature ($f_q^{\rm c}$, $h_q^{\rm fit}$, $B_q^{\rm fit}$, b) and one is T dependent (t'_σ). To determine ($f_q^{\rm c}$, $h_q^{\rm fit}$, $B_q^{\rm fit}$, b) it is best to work at low temperature so that the microscopic dynamics and α process are well separated and the time interval for the application of eq. (27) is large. Therefore, we fit the simulation data at the lowest temperature $T_{\rm min}$ where the TTSP still holds: $T_{\rm min} = 0.40$ for $N = 4$, $T_{\rm min} = 0.42$ for $N = 8$, $T_{\rm min} = 0.43$ for $N = 16$, and $T_{\rm min} = 0.44$ for $N = 32$ and 64. For these $T_{\rm min}$ we focus on $\phi_q(t)$ at $q = q_0 = 6.9$ near the maximum of $S(q)$ because the plateau of the two-step decay is high (cf. fig. 6), leading to a large range of ϕ values ($0 < \phi_{q_0} < f_{q_0}^{\rm c}$) where eq. (27) can be applied. Furthermore, a glance at fig. 8 shows that the decay of $\phi_{q_0}(t)$ roughly takes the same time for $N = 4$ and 64. This implies that we can employ the same fit interval $[t_{\rm min}, t_{\rm max}]$ for the different chain lengths. Since the choice of this interval has an influence on the numerical values of the fit parameters [66–68], we want to fix $[t_{\rm min}, t_{\rm max}]$ in the analysis. We choose the fit interval by two requirements: i) $t_{\rm min}$ should be larger than the time needed to complete the first relaxation step and ii) $t_{\rm max}$ should be much larger than $t_{\rm min}$, but not so large that the second-order correction in eq. (27) exceeds the von Schweidler law. In practice, we use the criterion $|B_{q_0}^{\rm fit}|(t_{\rm max}/t'_\sigma)^b < 0.4$. A possible choice [68] meeting these requirements is $[t_{\rm min}, t_{\rm max}] = [20, 500]$.

Using eq. (27) we then perform a five-parameter fit of $\phi_{q_0}(t)$ for all N. The fit is subject to several constraints: i) $f_q^{\rm c}$ must not be smaller than the value of $\phi_q(t)$ at the smallest times where the TTSP holds. Otherwise, eq. (15) would be violated. ii) The von Schweidler law $\sim h_q(t/t'_\sigma)^b$ is invariant under the rescaling $h_q \to \ell^b h_q$ and $t'_\sigma \to \ell t'_\sigma$ with ℓ being a constant. Therefore, the same fit result can be obtained for small t'_σ (small ℓ) or large t'_σ (large ℓ), if h_q changes accordingly. However, not all values of ℓ are acceptable. For instance, a very small value of ℓ could place t'_σ in the microscopic regime where the asymptotic formulas do not apply. To avoid such problems we have to constrain ℓ and for this, we need criteria for both h_q and t'_σ. In our analysis we first observe that fig. 4 imposes a lower bound on t'_σ because the von Schweidler law should hold only for $t \ll t'_\sigma$ (eq. (11)). So, t'_σ should be larger than the time interval where the factorization holds. For instance, for $N = 64$ at $T = 0.44$ this implies $t'_\sigma > 50$ (see fig. 4). Further guidance of the fit is obtained from results for hard-sphere systems [8, 52], which show that typical values of the critical amplitude near the maximum of $S(q)$ are $0.3 \lesssim h_q \lesssim 0.6$ [8]. So, we also require that h_{q_0} lies in these bounds.

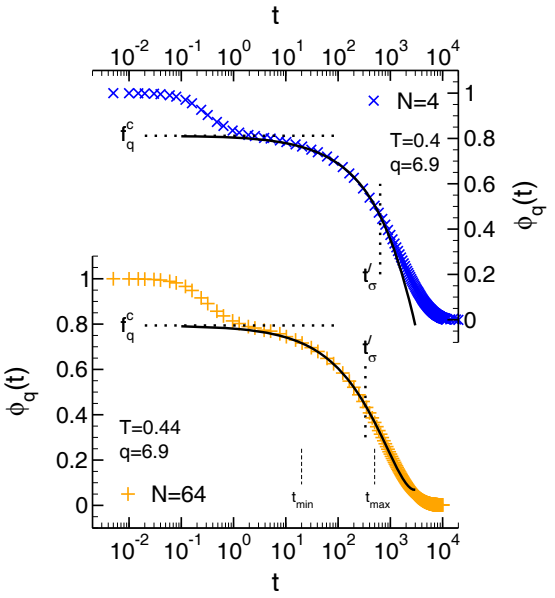

Fig. 8. $\phi_q(t)$ *versus* t for $q = 6.9$. The crosses (upper figure) show $\phi_q(t)$ for $N = 4$ at $T = 0.4$, the pluses (lower figure) depict $\phi_q(t)$ for $N = 64$ at $T = 0.44$. In both figures the solid lines present the results of the fit to eq. (27). The nonergodicity parameter ($f_q^{\rm c}$) and the α-relaxation time (t'_σ) are indicated, respectively, by a horizontal and a vertical dotted line. The time interval ($t_{\rm min} = 20 \le t \le t_{\rm max} = 500$) employed for the MCT fit is also shown (vertical dashed lines in the lower figure).

When applying this fit procedure we find that $f_{q_0}^{\rm c}$ is the quantity with the lowest standard deviation and slightly decreases with increasing N. Therefore we fix $f_{q_0}^{\rm c}$ for each N and go over to a four-parameter fit. This fit shows that the exponents b for different N agree within the error bars, for both coherent and incoherent scattering. So we also fix b at its average value ($b = 0.582$, cf. table 1) and carry out a three-parameter fit to get $h_{q_0}^{\rm fit}$, $B_{q_0}^{\rm fit}$ and $t'_\sigma(T_{\rm min})$ for each N. The remaining task is to determine (for each N) the q dependence of $h_q^{\rm fit}$, $B_q^{\rm fit}$ and the T dependence of t'_σ. For the q dependence we focus again on $T_{\rm min}$. Since we know the nonergodicity parameter for q_0, we can calculate $f_q^{\rm c}$ and $f_q^{\rm sc}$ for all other wave vectors because the relation $\phi_{q_0}(t_{\rm co}) = f_{q_0}^{\rm c}$ defines a crossover time $t_{\rm co}(T_{\rm min})$ where the t-dependent terms in eq. (27) vanish at $T_{\rm min}$. As $t_{\rm co}$ is independent of q, the nonergodicity parameters can be read off from the simulation data for any q value by $f_q^{\rm c} = \phi_q(t_{\rm co})$ and $f_q^{\rm sc} = \phi_q^{\rm s}(t_{\rm co})$. Fixing then $f_q^{\rm c}$ (or $f_q^{\rm sc}$),

b and $t'_\sigma(T_{\min})$ we carry out a two-parameter fit to get $h_q^{\rm fit}$, $B_q^{\rm fit}$ (and their incoherent counterparts). To get the T-dependence of t'_σ we focus again on q_0. We fix $f_{q_0}^{\rm c}$, $h_{q_0}^{\rm fit}$, $B_{q_0}^{\rm fit}$ and b, and fit $t'_\sigma(T)$ for all temperatures which obey the TTSP.

4.3.2 MCT calculations based on static input

MCT also suggests an alternative to fits with the asymptotic predictions. The full dynamics, addressing molecular details and preasymptotic corrections, can be calculated from the theory when accurate data for the static structure of the glass former are available. Comparisons of the dynamics predicted by such calculations with MD simulations were carried out in the past for various systems, including simple and molecular glass formers (see [52] and references therein) and bead-spring models for polymer melts [21,28,29]. The application to polymers employs an extension of the theory associating an interaction site with each monomer [20,21]. This extension provides an equation of motion for the collective density correlations, which is formally identical to the ideal MCT of atomic liquids. For the nonergodicity parameter (eq. (5)) the result reads

$$\frac{f_q}{1-f_q} = \frac{1}{2}\int {\rm d}^3\boldsymbol{k}\, V(\boldsymbol{q};\boldsymbol{k},\boldsymbol{p}) f_k f_p \tag{29}$$

with

$$V(\boldsymbol{q};\boldsymbol{k},\boldsymbol{p}) = \frac{\rho}{(2\pi)^3 q^2}\, S(q)S(k)S(p)\left\{\hat{\boldsymbol{q}}\cdot[\boldsymbol{k}c(k)+\boldsymbol{p}c(p)]\right\}^2, \tag{30}$$

where $\hat{\boldsymbol{q}} = \boldsymbol{q}/q$ and $\boldsymbol{p} = \boldsymbol{q}-\boldsymbol{k}$. Polymer-specific effects, such as chain stiffness [27–30] or chain length, enter into the theory only by the monomer density ρ, the structure factor $S(q)$ and the direct correlation function $c(q)$.

For $T > T_{\rm c,MCT}$ eq. (29) has only the solution $f_q(T) = 0$. (We use $T_{\rm c,MCT}$ for the critical temperature obtained from eq. (29) to discriminate it from the fit result to the asymptotic predictions; the latter is denoted by $T_{\rm c}$.) A vanishing nonergodicity parameter means that the correlations of density fluctuations decay to 0 for long times and the system is in a liquid state. By contrast, for $T \le T_{\rm c,MCT}$ eq. (29) yields $f_q(T) > 0$. Since the density fluctuations do not fully relax for $t \to \infty$, the system is in a glassy state. The MCT glass transition occurs at $T_{\rm c,MCT}$ where the nonergodicity parameter jumps from zero to its critical value $f_q(T_{\rm c,MCT}) = f_q^{\rm c} > 0$. This jump can be employed to calculate $T_{\rm c,MCT}$ and then also related quantities, such as h_q or λ.

If $T_{\rm c,MCT}$ lies in the T range for which equilibrated simulation data exist, the required static input can be determined (accurately) by interpolation. However, if $T_{\rm c,MCT}$ turns out to lie below the lowest equilibrated temperature, one has to resort to extrapolations. This problem was encountered in previous studies of polymeric glass formers [21, 28, 29] and is also found here. To estimate $S(q)$ we carry out a linear extrapolation from two low temperatures for each N: $T_1 = 0.38$ and $T_2 = 0.39$ for $N = 4$, $T_1 = 0.41$ and $T_2 = 0.42$ for $N = 8$, $T_1 = 0.42$ and $T_2 = 0.43$ for $N = 16$, $T_1 = 0.42$ and $T_2 = 0.43$ for $N = 32$, $T_1 = 0.44$ and $T_2 = 0.45$ for $N = 64$. As $w(q)$ is almost independent of T, no extrapolation needs to be performed, but $w(q)$ at T_1 is directly inserted into the MCT calculations. Similar procedures were also followed in [21,28,29]. Finally, the monomer density is extrapolated to low T by using the data from fig. 1.

To solve the MCT equations the interval $q \in [0.1, 50]$ is discretized in an equally spaced grid with $\Delta q = 0.2$ and the same numerical procedure as in ref. [52] is applied. The critical temperature $T_{\rm c,MCT}$ is obtained by a bisection algorithm with a precision (stop criterion) of 10^{-9}. The results of this calculation for the exponent parameter and the associated exponents (a, b, γ) turn out to be independent of chain length; they are included in table 1. The results for $T_{\rm c,MCT}$, $f_q^{\rm c}$ and h_q are discussed in the following section, together with the analysis of the MD data by the asymptotic MCT predictions.

4.3.3 MD and MCT: Discussion of the results

Figure 8 depicts simulation results (symbols) for $\phi_q(t)$ at $q = 6.9$, in the upper panel for $N = 4$ at $T = 0.4$ and in the lower panel for $N = 64$ at $T = 0.44$. Both temperatures correspond to the lowest T where the TTSP still holds at the respective chain length. At these temperatures we see that the coherent scattering functions for both N closely agree with one another: The height of the plateau is almost the same and the two-step decay roughly takes the same time. This shows that we can obtain a very similar $\phi_q(t)$ for small and large N, if a higher temperature is considered for large N. At a given T the main effect of increasing chain length is thus to slow down the local structural relaxation. Qualitatively, this observation may be correlated with the N dependence of the monomer density. From fig. 1 we know that the density at fixed T decreases with decreasing chain length. For small N lower temperatures should therefore be required to increase the density sufficiently so that the ensuing packing constraints lead to similar slow dynamics as for large N.

The solid lines in fig. 8 present the fits with eq. (27). The MCT curves describe the simulation data over about three decades in time and so also well outside the interval $[t_{\min}, t_{\max}]$ where the fit was performed. The fit starts to work already at rather short times ($t \gtrsim 5$), just after the first relaxation step. This first step is strongly influenced by the microscopic dynamics (*e.g.* Newtonian or stochastic [59, 69, 70]), hampering a test (by MD simulations) of the MCT predictions for the early β relaxation toward $f_q^{\rm c}$ [21, 52]. This problem is well known [6] and is the main reason why we employ the MCT prediction (27) for the late β process in our analysis, as other studies on nonpolymeric [52,63,65,71,72] and polymeric liquids [27, 28, 30–33] have done too. From the fits with eq. (27) we find an N-independent value for the von Schweidler exponent $b = 0.583$, which implies an exponent parameter $\lambda = 0.735$. This λ value agrees with the

result for hard spheres [8,9,52] and is characteristic of low-molecular weight glass-forming liquids (*e.g.* binary mixtures [58, 64, 65, 73–75], models for water [71], silica [63] and *ortho*-terphenyl [72,76]) or other fully flexible polymer models [21, 27, 28], but not for stiffer bead-spring models with strong torsional barriers [27–29] or chemically realistic polymer models [30–33] where typically larger values $\lambda \sim 0.9$ (and, along with that, stronger stretching of the late β process, $b \sim 0.3$) are found. Prompted by other MCT results [17] it has been argued [27, 28, 31–33] that such large λ values could be caused by the simultaneous occurrence of two mechanisms of dynamic arrest in such polymer systems: intermolecular packing, operating also in simple glass formers, and intramolecular barriers for conformational transitions, a polymer-specific effect. The present finding that λ is independent of N and has a standard value for simple liquids—a finding that is corroborated by the MCT calculations based on the static input (cf. table 1)—suggests that the increase of the chain length does not introduce an additional mechanism for glass-like arrest, at least for fully flexible polymer models and in the range of nonentangled chains studied here.

The fits by eq. (27) also provide the q-dependence of $f_q^{\rm c}$, h_q, B_q and of their incoherent counterparts. Figures 9, 10 and 11 depict the results. The found q-dependence has many features that agree qualitatively with theoretical predictions [8, 9] and other simulations [21, 35, 52, 60, 63, 65, 71–74, 76]:

i) For $q \gtrsim q^*$ the nonergodicity parameter $f_q^{\rm c}$ closely follows the oscillations of $S(q)$ (fig. 9), whereas the critical amplitude h_q and the long-time correction coefficient B_q are roughly in antiphase with $f_q^{\rm c}$ for $q \lesssim 10$ (figs. 10, 11). From fig. 9 we also see that $f_q^{\rm c} \approx f_q^{\rm sc}$ for $q \gtrsim 11$. The agreement between coherent and incoherent scattering becomes better with increasing q. Similar agreement between coherent and incoherent scattering is also obtained for h_q, $h_q^{\rm s}$ (fig. 10) and B_q, $B_q^{\rm s}$ (fig. 11).

When comparing $f_q^{\rm c}$ and h_q from the fits and the MCT calculations based on static input (fig. 9(a), (c); fig. 10(a), (b)) we see that both analyses yield qualitatively the same q dependence for $q \gtrsim q^*$. However, $f_q^{\rm c}$ and h_q from the MCT calculations are typically larger than the fit results and the dependence on N is more pronounced in the calculations than in the fits.

ii) For the incoherent scattering the nonergodicity parameter $f_q^{\rm sc}$ monotonically decreases with q. For small q one expects the Gaussian approximation,

$$f_q^{\rm sc} = \exp(-q^2 r_{\rm sc}^2), \tag{31}$$

to hold, with $r_{\rm sc}$ being the "Lindemann localization length" [9]. Fitting this relation for $q \leq 3$ to our simulation data results in $0.0853 \lesssim r_{\rm sc} \lesssim 0.0863$ for all N. This variation with N is so weak that we average the values to get $r_{\rm sc} = 0.0858$. This average localization length is about 10% of the monomer diameter, as suggested by MCT [9]. The dash-dotted line in fig. 9 shows eq. (31) with $r_{\rm sc} = 0.0858$ and gives a good description of the MD data for $q \lesssim 8$.

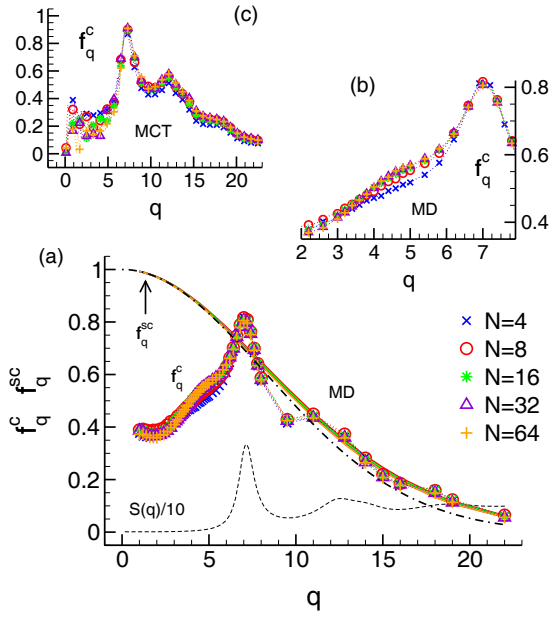

Fig. 9. Panel (a): Nonergodicity parameter for coherent scattering ($f_q^{\rm c}$; symbols) and incoherent scattering ($f_q^{\rm sc}$; lines) *versus* q for different N as obtained by fitting eq. (27) to the MD data. For comparison $S(q)$ (divided by 10) is shown by a dashed line; $f_q^{\rm c}$ is in phase with $S(q)$ for $q \gtrsim q^*$. The dash-dotted line represents the Gaussian approximation for $f_q^{\rm sc}$ (eq. (31)) with $r_{\rm sc} = 0.0858$. This value is obtained as an average when fitting eq. (31) to $f_q^{\rm sc}$ for $q \leq 3$ (yielding $0.0853 \lesssim r_{\rm sc} \lesssim 0.0863$ for all N studied). Panel (b): Zoom of the N-dependent shoulder occurring in the simulation data for $f_q^{\rm c}$ in the range of $4 \lesssim q \lesssim 6$. Panel (c): Results for $f_q^{\rm c}$ from the MCT calculations based on the static input. The symbols for the different N are the same as in panel (a).

iii) Similar Gaussian approximations are also known for the critical amplitude and long-time correction coefficient. They are expected to describe the initial increase of $h_q^{\rm s}$ and $B_q^{\rm s}$ for small q [9]. For $h_q^{\rm s}$ the approximation reads

$$h_q^{\rm s} = h_{\rm msd} q^2 \exp(-q^2 r_{\rm sc}^2), \tag{32}$$

where $h_{\rm msd}$ is a constant. To get $h_{\rm msd}$ we fit eq. (32) with $r_{\rm sc} = 0.0858$ to the MD data for $q \leq 3$. Again the N dependence of $h_{\rm msd}$ turns out to be weak. Averaging gives $h_{\rm msd} = 0.0221$. This result is shown as a dash-dotted line in fig. 10; it describes the simulation data well only for $q < 4$, so for a smaller q range than in the case of $f_q^{\rm sc}$. This decrease of the q interval for the applicability of the Gaussian approximation is expected from hard-sphere calculations and should continue for the long-time correction amplitude $B_q^{\rm s}$ [9]. Indeed, we found that the Gaussian approximation for $B_q^{\rm s}$ cannot be fitted to our simulation data. The $q \to 0$ limit $B_0^{\rm s}$ shown in fig. 11 was obtained from an analysis of the monomer mean-square displacement (MSD) to which we will turn below.

Before doing so we want to comment on the behavior of the coherent quantities $f_q^{\rm c}$, h_q, B_q for $q < q^*$. Figures 9, 10 and 11 show that $f_q^{\rm c}$ exhibits a shoulder at $q \approx 4.5$, whereas h_q has a pronounced minimum and B_q

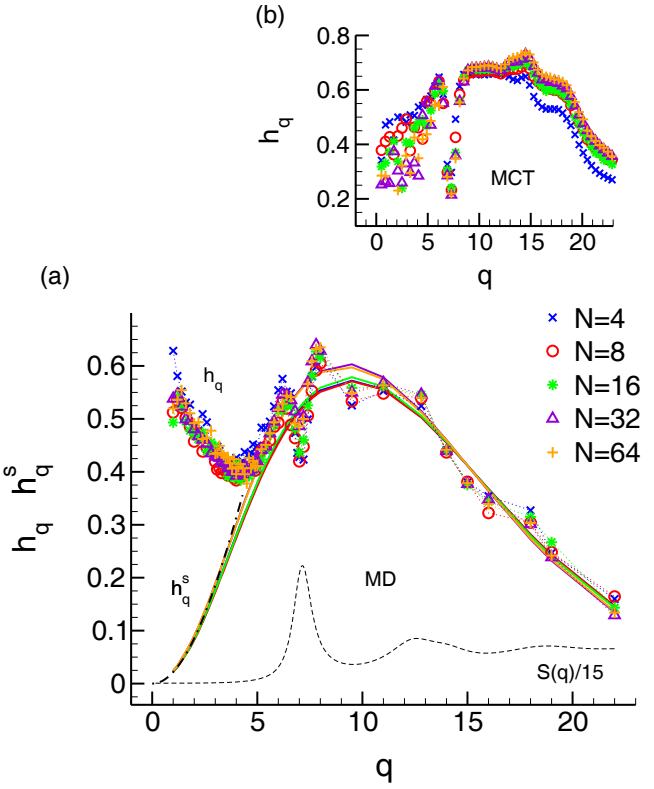

Fig. 10. Panel (a): Critical amplitude for coherent scattering (h_q; symbols) and incoherent scattering (h_q^s; lines) *versus* q for different N. For comparison $S(q)$ (divided by 15) is shown by a dashed line; h_q is in antiphase with $S(q)$ for $q \sim q^*$. The dash-dotted line represents the Gaussian approximation for h_q^s (eq. (32)) with $r_{sc} = 0.0858$ from fig. 9 and $h_{msd} = 0.0221$. This value is obtained as an average when fitting eq. (32) to h_q^s for $q \leq 3$ (yielding $0.0213 \lesssim h_q^s \lesssim 0.0228$ for all N studied). Panel (b): Results for h_q from the MCT calculations based on the static input. The symbols for the different N are the same as in panel (a).

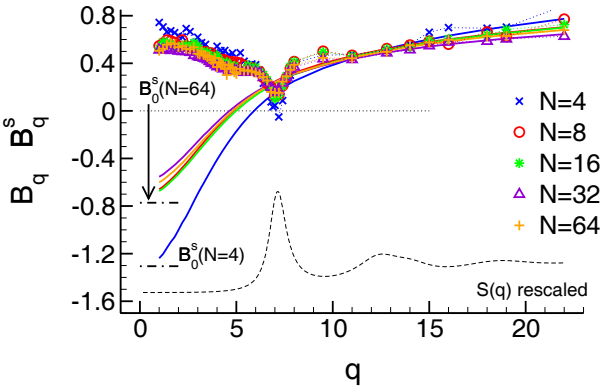

Fig. 11. Long-time correction coefficient for coherent scattering (B_q; symbols) and incoherent scattering (B_q^s; lines) *versus* q for different N. For comparison $S(q)$ (rescaled) is shown by a dashed line; B_q is in antiphase with $S(q)$ for $q \gtrsim q^*$. For $N = 4$ and 64 the vertical dash-dotted lines represent the limiting values of B_q^s for $q \to 0$ obtained from a fit of eq. (34) to the mean-square displacement of the monomers (cf. figs. 12 and 13).

a dip in this q range. These features have no parallel in $S(q)$, are absent in hard-sphere systems [8,52] and in the MCT calculations utilizing the static input (fig. 9(c) and fig. 10(b)), but are observed in many simulations of polymer models [21,28–30,35]. In [35] it was conjectured that these features could be correlated with the dynamic coupling of the chains' centers of mass (CMs). This conjecture was motivated by the observation that the position of the shoulder in f_q^c almost coincided with $2\pi/R_g$ where R_g is the radius of gyration of the $N = 10$ system studied in [35]. However, the more recent studies [21,28–30], including the present one, suggest that this conjecture is not correct. First, the position of the shoulder should shift to smaller q, if R_g increases, *e.g.*, by increasing chain stiffness or chain length. The work of [28,29] however shows that the shoulder does not shift in q when chain stiffness is varied. The same observation is made here for the variation of the chain length. Only the amplitude of the shoulder is affected by N, apparently approaching an asymptotic limit for $N > 8$ (see inset of fig. 9). A further argument against the proposed correlation with the CM dynamics comes from MCT calculations for fully flexible polymer models [21,28,29] and models with intramolecular barriers [28,29]. In their common form, these calculations associate interaction sites with each monomer and employ two-point static correlation functions, *i.e.* $S(q)$, $w(q)$ and $c(q)$, to derive the dynamics of the system. However, such MCT approaches find (practically) no influence of chain stiffness on f_q^c for $q < q^*$ [28] and also strongly underestimate the nonergodicity parameter for $q \approx 4.5$ [21,28]. It is possible to include the CM as a further interaction site in the calculations. However, no improvement was obtained for fully flexible chains [21] and is also unlikely for the models with intramolecular barriers because the static structure factor of the CMs is already close to 1 for $q \approx 4.5$ [29]. So the static coupling of the CMs is very weak in the pertinent q range [21]. Apparently, polymer melts have slow collective modes [21,28–30] in an intermediate q range ($q \approx 0.6q^*$) which do not have a static fingerprint in standard two-point correlation functions.

Let us now turn to the time dependence of $\phi_q^s(t)$ and of the monomer MSD $g_0(t)$. Both quantities are related in the limit $q \to 0$ where the Gaussian approximation

$$\phi_q^s(t) = \exp\left[-\frac{1}{6}q^2 g_0(t)\right] \tag{33}$$

holds. This relation was utilized in [9] to obtain the MCT prediction for the MSD in the late β regime

$$g_0(t) = 6r_{sc}^2 + 6h_{msd}B\left(\frac{t}{t'_\sigma}\right)^b - 6h_{msd}B^2B_0^s\left(\frac{t}{t'_\sigma}\right)^{2b} \tag{34}$$

with the Lindemann localization length r_{sc} (eq. (31)), the critical amplitude h_{msd} (eq. (32)), and the long-time correction coefficient $B_0^s = \lim_{q\to 0} B_q^s$ (eq. (13)). For times longer the late β regime polymer-specific correlations due to chain connectivity will determine the monomer dynamics. If the chains are nonentangled (as in our case), the Rouse model [37,38] can be expected to represent a good

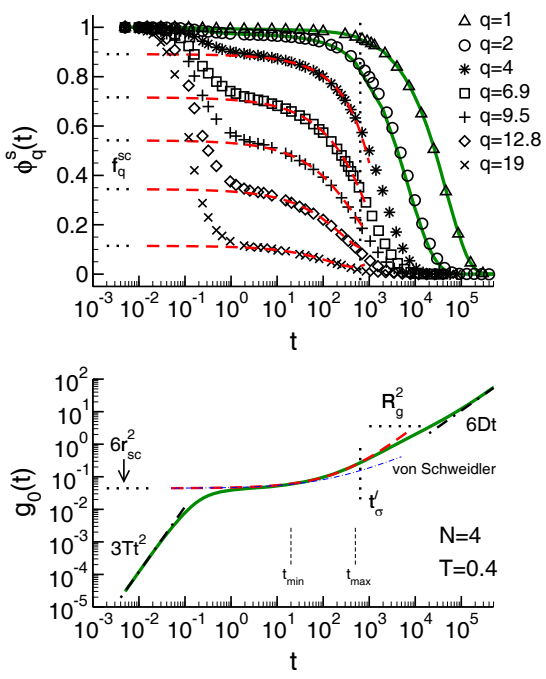

Fig. 12. Incoherent scattering function $\phi_q^s(t)$ and monomer MSD $g_0(t)$ for $N = 4$ at $T = 0.4$. In the upper panel the symbols depict $\phi_q^s(t)$ for different q. For $q = 1$ and 2 the solid lines represent the Gaussian approximation (33) with the $g_0(t)$ obtained from the simulation. For the other wave vectors the dashed lines show the results from eq. (27) with the MCT parameters from figs. 9, 10, and 11. The horizontal dotted lines indicate f_q^{sc}; the vertical dotted line indicates t'_σ. In the lower panel the solid line represents $g_0(t)$. The ballistic ($g_0(t) = 3Tt^2$) and diffusive behaviors ($g_0(t) = 6Dt$) are indicated by dash-dotted lines. The (red) dashed line depicts the MCT prediction, eq. (34). Here we used $r_{sc} = 0.0858$ from fig. 9 and $h_{msd} = 0.0221$ from fig. 10, whereas B_0^s ($= -1.3055$) was obtained by fitting eq. (34) to $g_0(t)$ in the interval $t_{min} = 20 \le t \le t_{max} = 500$. The (blue) dash-dotted line shows the von Schweidler law, *i.e.* eq. (34) with $B_0^s = 0$. The horizontal dotted lines show the nonergodicity parameter ($6r_{sc}^2$) of $g_0(t)$ and the radius of gyration of the chains ($R_g^2 = 3.578$). The vertical dotted line indicates t'_σ.

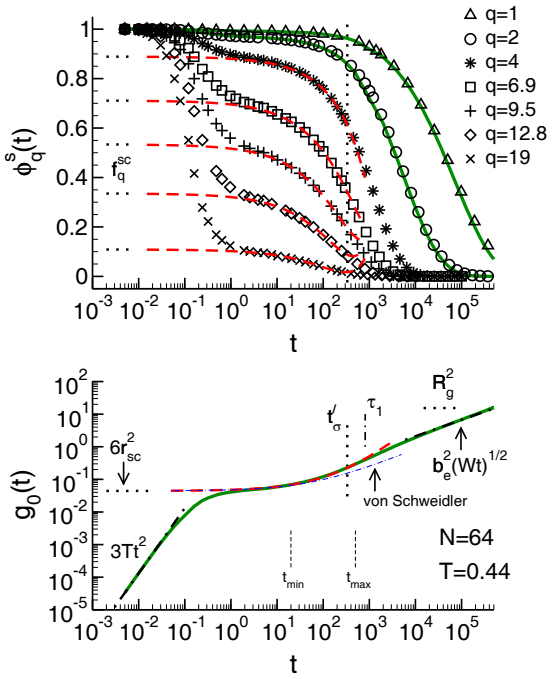

Fig. 13. Incoherent scattering function $\phi_q^s(t)$ and monomer MSD $g_0(t)$ for $N = 64$ at $T = 0.44$. In the upper panel the symbols depict $\phi_q^s(t)$ for different q. For $q = 1$ and 2 the solid lines represent the Gaussian approximation (33) with the $g_0(t)$ obtained from the simulation. For the other wave vectors the dashed lines show the results from eq. (27) with the MCT parameters from figs. 9, 10, and 11. The horizontal dotted lines indicate f_q^{sc}; the vertical dotted line indicates t'_σ. In the lower panel the solid line represents $g_0(t)$. The ballistic behavior ($g_0(t) = 3Tt^2$) and the prediction from the Rouse model ($g_0(t) = b_e^2\sqrt{Wt}$) are indicated by dash-dotted lines. For the Rouse model we used $b_e = 1.295$ from ref. [68] and fitted $W = 1.586 \times 10^{-4}$. For the monomer relaxation time of the Rouse model this gives $\tau_1 = 4/(\pi^3 W) = 813.4$ (shown by a vertical dash-dotted line). The (red) dashed line depicts the MCT prediction, eq. (34). Here we used $r_{sc} = 0.0858$ from fig. 9 and $h_{msd} = 0.0221$ from fig. 10, whereas B_0^s ($= -0.7724$) was obtained by fitting eq. (34) to $g_0(t)$ in the interval $t_{min} = 20 \le t \le t_{max} = 500$. The (blue) dash-dotted line shows the von Schweidler law, *i.e.* eq. (34) with $B_0^s = 0$. The horizontal dotted lines show the nonergodicity parameter ($6r_{sc}^2$) of $g_0(t)$ and the radius of gyration of the chains ($R_g^2 = 15.39$). The vertical dotted line indicates t'_σ.

approximation [77–79]. The Rouse model predicts [37,38]

$$g_0(t) = b_e^2\sqrt{Wt}, \qquad \tau_1 < t < \tau_N. \tag{35}$$

with

$$\tau_1 = \frac{4}{\pi^3 W} \quad \text{and} \quad \tau_N = \tau_1 N^2. \tag{36}$$

Here b_e denotes the effective bond length, W the monomer relaxation rate, τ_1 the monomer relaxation time and τ_N the Rouse time. For $t > \tau_N$ this subdiffusive motion crosses over to normal diffusion where $g_0(t) = 6Dt$ with D being the diffusion coefficient of the polymer. Equations (33)–(36) will be compared to the MD data in the following.

Figure 12 depicts $\phi_q^s(t)$ (upper panel) and $g_0(t)$ (lower panel) for $N = 4$ at $T = 0.4$, whereas fig. 13 shows the same data for $N = 64$ at $T = 0.44$. For both chain lengths $g_0(t)$ starts from the ballistic regime ($3Tt^2$) and goes over to a plateau. The height of the plateau gives an estimate of the localization length for a monomer which is temporarily trapped in the cage of its neighbors. Figures 12 and 13 show that the value $r_{sc} = 0.0858$, obtained from the fit in fig. 9, is consistent with the height of the plateau. Moreover, the figures also show that the MCT prediction (34) allows to describe the increase of $g_0(t)$ beyond the plateau over about three decades for both N. Here only B_0^s was fitted, all other quantities were taken from the previous analysis. The fits give $B_0^s = -1.3055$ for $N = 4$ and $B_0^s = -0.7724$ for $N = 64$. This N dependence may be understood as follows: For $N = 4$ the

chains are too short to display subdiffusive Rouse motion and the MSD quickly becomes diffusive (fig. 12). For $N = 4$ the MSD thus increases more steeply with t than for $N = 64$ where the increase of $g_0(t)$ flattens so that the α-process can merge with eq. (35) (fig. 13). Therefore, the von Schweidler law underestimates the increase of $g_0(t)$ more strongly for $N = 4$ than for $N = 64$ (compare figs. 12 and 13). To compensate this underestimation the fit with eq. (34) yields a larger $|B_0^{\rm s}|$ for $N = 4$ than for $N = 64$. This also explains why the long-time correction coefficient $B_q^{\rm s}$ has a pronounced dependence on N for $q < q^*$, as shown in fig. 11.

The upper panel of figs. 12 and 13 shows $\phi_q^{\rm s}(t)$ for $1 \leq q \leq 19$. For both chain lengths and all q values $\phi_q^{\rm s}(t)$ exhibits a two-step relaxation. If $q \lesssim 2$, the Gaussian approximation (33) with $g_0(t)$ taken from the simulation represents a good approximation for $\phi_q^{\rm s}(t)$ (green solid lines). For larger q the incoherent correlators can be described over more than two decades by eq. (27) with the values for b and t'_σ determined before from the analysis of coherent scattering function. Similar consistency is also found for other temperatures (where the TTSP holds) and for all chain lengths.

The fits provide the α-relaxation time $t'_\sigma(T)$ for all N. According to eq. (8) a plot of $t_\sigma'^{-1/\gamma}$ *versus* T, with γ calculated from b by eqs. (8) and (9), should give a straight line that extrapolates to 0 at $T_{\rm c}(N)$. This prediction is tested in fig. 14. Indeed, we find straight lines which shift to larger T with increasing N and furthermore are parallel to each other (with the exception of $N = 8$ where a slight deviation from parallelism occurs). This implies that $T_{\rm c}$ increases with N and that the prefactor t_0/C^γ, linking t'_σ to $(T-T_{\rm c})/T_{\rm c}$, is independent of N. A master curve should therefore be obtained by plotting the α-relaxation time *versus* $(T - T_{\rm c})/T_{\rm c}$. This is confirmed in the lower panel of fig. 14, not only for t'_σ but also for τ_{q_0}, the scaling time used in the test of the TTSP (cf. fig. 6). Since τ_{q_0} is read off from the simulation data (by $\phi_{q_0}(\tau_{q_0}) = 0.1$), it can be determined also for temperatures below $T_{\rm min}$ where the β analysis was performed. Figure 14 shows that the scaling with $T_{\rm c}$ onto an N independent master curve continues to work down to the lowest T studied (and even below $T_{\rm c}$) where τ_{q_0} displays clear deviations from the straight-line behavior and the mode-coupling transition is avoided.

The extrapolated $T_{\rm c}$ resulting from the fit in fig. 14 is compiled in table 1 and plotted *versus* N in fig. 15(a). We find that the increase of $T_{\rm c}$ with N can be fitted by

$$T_{\rm c}(N) = T_{\rm c}^\infty - \frac{C_{\rm c}}{N}\,, \qquad (37)$$

where $T_{\rm c}^\infty$ is the critical temperature for infinite chain length and $C_{\rm c}$ is a constant. Based on free-volume arguments the same N dependence was first suggested by Fox and Flory for the glass transition temperature $T_{\rm g}$ [49,80]. Although the Fox-Flory approach has been criticized (see, *e.g.*, [81]) and other functional forms were discussed in the recent literature [82–84], eq. (37) is often used to model experimental [81,83] or simulation data for $T_{\rm g}$ [85,86]. We have done so too in [39] where the same polymer model

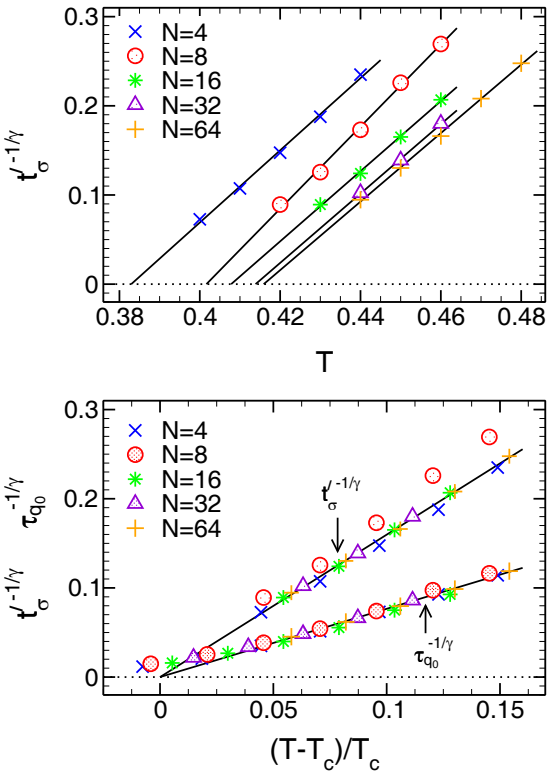

Fig. 14. Upper panel: Rectification plot of t'_σ (symbols) *versus* T for different N. The value of γ (= 2.464) is taken from table 1. The solid lines are fits to eq. (8) to determine $T_{\rm c}(N)$. Lower panel: Plot of $t_\sigma'^{-1/\gamma}$ and $\tau_{q_0}^{-1/\gamma}$ *versus* $(T - T_{\rm c})/T_{\rm c}$. τ_{q_0} is taken from figs. 6 and 7 ($q_0 = 6.9$). The scaling with N indicates that the prefactors, t_0/C^γ in eq. (8) and C_{q_0} in eq. (16), can be taken as independent of chain length in very good approximation.

was studied as in this work, albeit at higher pressure, and $T_{\rm g}$ was determined from dilatometry in continuous cooling runs with a finite rate. The crosses in fig. 15 show the resulting $T_{\rm g}$ values (multiplied by a constant factor to put them on the scale of the figure). Interestingly, the N dependence of $T_{\rm c}$, extrapolated from equilibrium data, and of $T_{\rm g}$ from the nonequilibrium simulations of [39] agree with each other very well.

The squares in fig. 15(a) depict the estimates for $T_{\rm c,HV}$ from the Hansen-Verlet criterion (cf. table 1). As pointed out in sect. 4.1, application of this criterion suggests $T_{\rm c}$ to decrease with increasing N, and so the opposite trend as obtained from the MCT fits. Although the Hansen-Verlet criterion is a crude approach and wave vectors larger than q^* also contribute strongly to the integral (29) [52], the MCT calculation employing the static input from the simulation gives qualitatively the same N dependence as the Hansen-Verlet criterion (cf. fig. 15(b)). In addition to this difference between MCT and simulation the theory also predicts much smaller values for $T_{\rm c}$ (compare fig. 15(a) and (b)). This disagreement might be related to the differences in $f_q^{\rm c}$ for $q \approx 4.5$ where the MD data display an N dependent shoulder that is absent in the MCT calculation (cf. fig. 9). This shoulder corresponds to slow collective density

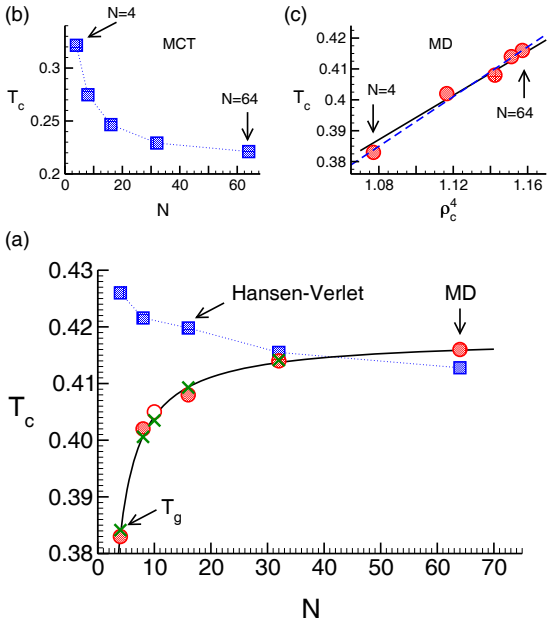

Fig. 15. Panel (a): T_c *versus* N (filled circles). T_c is determined from the extrapolation of t'_σ in fig. 14. The solid line shows a fit to eq. (37) with $T_c^\infty = 0.418$ and $C_c = 0.139$. The open circle corresponds to $T_c = 0.405$ for $N = 10$ found in [43]. The crosses present the results for the glass transition temperature T_g obtained in [39] from continuous cooling runs (with rate $\Gamma_T = 2 \times 10^{-5}$) at pressure $P = 1$; the data are scaled by 0.968 ($= T_c^\infty/T_g^\infty$ with $T_g^\infty = 0.432$ [39]). The squares show the estimates for T_c obtained from the Hansen-Verlet criterion (denoted by $T_{c,HV}$ in table 1), *i.e.*, from $S(q^*, T_c) = 3.54$. The blue dotted line through the data is a guide to the eye. Panel (b): Chain-length dependence of $T_{c,MCT}$ obtained from the MCT calculations using the static input from the simulation. The data are taken from table 1. Panel (c): T_c from panel (a) *versus* ρ_c^4 (filled circles). The values for ρ_c are taken from table 1. The linear regression (solid line) gives $\Gamma_c^{-4} = 0.358$, *i.e.*, $\Gamma_c = 1.29$. The (blue) dashed line shows a best fit to the data, yielding $T_c(\rho_c) = 0.353\rho_c^{4.5}$.

fluctuations which could couple to the relaxation at other wave vectors in eq. (29). Within the theory the only way to compensate for these slow modes is to make the cage effect stronger by increasing $S(q)$ for $q \gtrsim q^*$ through a decrease of $T_{c,MCT}$.

Finally, we want to discuss the correlation between T_c and the monomer density (see also [42] for a similar discussion). Figure 1 shows that the density increases with N as $\rho_\infty - \rho(N) \sim 1/N$. Qualitatively, this agrees with eq. (37). So the increase of T_c may be interpreted as resulting from the monomer density. A similar increase of T_c with ρ is observed for simple LJ liquids [75,87] and can be rationalized as follows. LJ liquids are strongly correlating systems displaying *e.g.* strong pressure-energy correlations [88] or density scaling of the average relaxation time [88,89] (*i.e.* the average relaxation time is only a function of the scaling variable ρ^γ/T with γ being a material-specific exponent [90]). These features may be understood by mapping the LJ liquid on an effective soft-sphere system [87–89, 91]. A soft-sphere system is characterized by the coupling parameter $\Gamma = \rho T^{-3/n}$, if the repulsive pair-potential varies as r^{-n} with the interparticle distance r [92]. Due to the repulsive part of the LJ potential a natural guess is that $n = 12$. This suggests $\Gamma_c = \rho_c {T_c}^{-1/4}$ where $\rho_c = \rho(T_c)$ [87]. We have determined ρ_c for all N from the data in fig. 1 and plot T_c *versus* ρ_c^4 in the inset of fig. 15. The solid line in fig. 15 shows that the data are compatible with a linear relationship, yielding $\Gamma_c = 1.29$. Within error bars this value agrees with the result $\Gamma_c = 1.27 \pm 0.02$ found in simulations at different pressure for fully flexible polymer models with $N = 10$ ($P = 0$ [43], $P = 0.5, 1, 2$ [93]). On the other hand, a best fit of the data gives $T_c \sim \rho_c^{4.5}$ (dashed line in the inset of fig. 15), corresponding to $n = 13.5$. Exponents larger than $n = 12$ are also found for LJ liquids and explained by the contribution of the attractive r^{-6} term which makes the effective repulsion steeper [88, 89]. However, the reported values are larger than $n = 13.5$, typically $n \approx 15$ [89] or $n \approx 18$ [88].

5 Summary and concluding remarks

In this work we conducted MD simulations of a fully flexible bead-spring model for polymer melts and examined the structural relaxation of the supercooled melt as a function of chain length. Coherent and incoherent correlators were analyzed by the universal predictions of ideal MCT for the β and α relaxations (sect. 3). These predictions are expected to hold asymptotically close to the critical temperature on approach to T_c from above. While qualitative features, *i.e.* the validity of the factorization theorem and of the TTSP, can be tested directly from the simulation data (sect. 4.2), the quantitative analysis in the late β regime requires fits which are complicated by two problems: i) Choices for the time interval and temperature, where the fit will be carried out, have to be made. They can bias the results. ii) The fit has to optimize five parameters simultaneously. Correlations between the parameters are therefore hard to avoid. These problems are well known in the literature [66, 67, 94, 95]. Any fit procedure can only attempt to minimize them. Our approach is described in sect. 4.3.1.

The fits in the late β regime give detailed insight into chain-length dependence of the structural relaxation near T_c. Here we summarize our findings and put them into perspective with other work:

i) The nonergodicity parameter (f_q^{sc}) for the incoherent scattering can be taken as independent of N (fig. 9). This implies that also the Lindemann localization length (r_{sc}) does not depend on chain length. We obtain for r_{sc} a value of about 10% of the particle (monomer) diameter, also typically found in simple liquids [9,58] and other fully flexible polymer models [21, 27, 28, 34]. However, stiffer bead-spring models with intramolecular barriers [27,28] or chemically realistic models [32,33] report deviations from the Lindemann's 10% value, depending on the strength of the intramolecular barrier or on the atom considered along

the real chain (see [33] for a comparative discussion). For these cases it would be interesting to see whether chain length also has a negligible effect only.

ii) Contrary to f_q^{sc} the long-time correction coefficient (B_q^s) for the incoherent scattering shows a pronounced N dependence in the limit of small q (fig. 11). This can be rationalized by the fact that B_0^s, the correction coefficient entering the monomer MSD, is determined in the crossover region between the escape from the monomer cage and the subdiffusive regime ($\sim t^x$) caused by chain connectivity. For short chains the exponent x is larger than the Rouse value $x = 1/2$ [7, 21, 96], but decreases toward 1/2 with increasing chain length (compare fig. 12 and 13). This N dependence is reflected by B_q^s in the small-q limit.

iii) For the coherent scattering a particular feature is the shoulder in f_q^c at $q \approx 4.5 \approx 0.6q^*$. This feature is absent in simple liquids [8,52], but found in many simulations of polymer models [21,27,28,30,35]. Work on models with intramolecular barriers shows that the amplitude of the shoulder converges with increasing chain stiffness toward a smaller value than for fully flexible chains [27,28]. Here we find the opposite trend. The amplitude increases for small chain lengths, but converges to an N independent value for the largest chain lengths studied. These results show that there are polymer-specific (stiffness and chain-length dependent) slow modes in the collective density fluctuations at intermediate wave vectors. These slow modes are not captured by (current) MCT calculations based on static input from the simulations (cf. fig. 9 and [21,28,29]). This may be the reason why such calculations systematically underestimate T_c (see fig. 15 and [21, 28, 29]), contrary to similar calculations for binary mixtures [52, 64, 65, 74], silica [97] or *ortho*-terphenyl [98], which yield larger T_c values than the fits to the asymptotic MCT predictions. The studies on silica and *ortho*-terphenyl also hint at another possibility of how to improve on the theoretical calculations. As in [21] the MCT calculation carried out here neglect static three-point correlations that in principle enter the MCT kernel (eq. (30)) as an additional term. For silica [97] and *ortho*-terphenyl [98] these correlations considerably increase T_c (while they are negligible for binary mixtures [97]). Prompted by these results recent work on bead-spring models with intrachain barriers included the triplet correlations at the intramolecular level [29]. However, only very small modifications of the MCT predictions were found.

iv) Consistent with the expectation from MCT we find that one exponent parameter λ determines the shape of the coherent and incoherent scattering functions. Our analysis suggests that λ is independent of N and has a typical value $\lambda = 0.735$ as for simple liquids [8,9,52,58,65,73, 74] and other fully flexible polymer models [21, 27, 28]. By contrast, work on chemical realistic models [30–33] and bead-spring models with large intramolecular barriers [27–29] obtains higher λ values approaching the upper limit $\lambda = 1$. Within MCT such large λ values are indicative of the simultaneous occurrence of competing mechanisms for dynamic arrest [3,17]. For polymer melts it has been suggested that these mechanisms could correspond to packing effects, as in simple liquids, and polymer-specific intramolecular barriers [27–29, 31–33]. In this sense, our work suggests that the increase of chain length does not introduce an additional arrest mechanism, at least for the nonentangled chains studied here.

v) The studies of the bead-spring models with intramolecular barriers show that T_c increases with chain stiffness [27–29]. For the fully flexible model we find here that T_c increases with chain length toward an upper limit T_c^∞. The increase is comparable to that of T_g [39] and may be parameterized by $T_c^\infty - T_c \sim 1/N$ (fig. 15). This effect can be understood from the behavior of the monomer density [42] by assuming that our polymer model corresponds to an effective soft-sphere system characterized by a constant coupling parameter $\Gamma_c = \rho_c {T_c}^{-1/4} = 1.29$. This argument has also been employed in the past to interpret the pressure dependence of T_c [43, 93]. This suggests that fully flexible LJ polymer models belong to the class of "strongly correlating" liquids which have invariant structure and dynamics along specific curves ("isomorphs") in the ρ-T plane [88]. It would be interesting to explore this suggestion in more detail.

We are indebted to S.-H. Chong and Th. Voigtmann for many helpful discussions. We thank O. Benzerara for continued technical support during this work. We gratefully acknowledge financial support from the MESR, the IRTG "Soft Matter Science" and the DAAD.

References

1. W. Götze, L. Sjögren, Rep. Prog. Phys. **55**, 241 (1992).
2. W. Götze, J. Phys.: Condens. Matter **11**, A1 (1999).
3. W. Götze, *Complex Dynamics of Glass-Forming Liquids: A Mode-Coupling Theory* (Oxford University Press, Oxford, 2009).
4. A. Cavagna, Phys. Rep. **476**, 51 (2009).
5. L. Berthier, G. Biroli, Rev. Mod. Phys. **83**, 587 (2011).
6. W. Kob, in *Slow relaxations and nonequilibrium dynamics in condensed matter*, edited by J.L. Barrat, M. Feigelmann, J. Kurchan, J. Dalibard (EDP Sciences/Springer, Les Ulis/Berlin, 2003) pp. 201–269.
7. J. Baschnagel, F. Varnik, J. Phys.: Condens. Matter **17**, R851 (2005).
8. T. Franosch, M. Fuchs, W. Götze, M.R. Mayr, A.P. Singh, Phys. Rev. E **55**, 7153 (1997).
9. M. Fuchs, W. Götze, M.R. Mayr, Phys. Rev. E **58**, 3384 (1998).
10. W. Götze, L. Sjögren, Transport Theory Stat. Phys. **24**, 801 (1995).
11. M.E. Cates, S. Ramaswamy, Phys. Rev. Lett. **96**, 135701 (2006).
12. P. Meyer, K. Miyazaki, D. Reichman, Phys. Rev. Lett. **97**, 095702 (2006).
13. S.H. Chong, Phys. Rev. E **78**, 041501 (2008).
14. K.S. Schweizer, Curr. Opinion Coll. Interf. Sci. **12**, 297 (2007).
15. A.S. Keys, L.O. Hedges, J.P. Garrahan, S.C. Glotzer, D. Chandler, Phys. Rev. X **1**, 021013 (2011).

16. K.N. Pham, A.M. Puertas, J. Bergenholtz, S.U. Egelhaaf, P.N. Moussaïd, P.N. Pusey, A.B. Schofield, M.E. Cates, M. Fuchs, W.C.K. Poon, Science **269**, 104 (2002).
17. M. Sperl, Phys. Rev. E **68**, 031405 (2003).
18. A.J. Moreno, J. Colmenero, Phys. Rev. E **74**, 021409 (2006).
19. A.J. Moreno, J. Colmenero, J. Chem. Phys. **124**, 184906 (2006).
20. S.H. Chong, M. Fuchs, Phys. Rev. Lett. **88**, 185702 (2002).
21. S.H. Chong, M. Aichele, H. Meyer, M. Fuchs, J. Baschnagel, Phys. Rev. E **76**, 051806 (2007).
22. V. Krakoviack, Phys. Rev. E **75**, 031503 (2007).
23. V. Krakoviack, Phys. Rev. E **79**, 061501 (2009).
24. V. Krakoviack, Phys. Rev. E **84**, 050501(R) (2011).
25. S. Lang, R. Schilling, V. Krakoviack, T. Franosch, Phys. Rev. E **86**, 021502 (2012).
26. M. Fuchs, Adv. Polym. Sci. **236**, 55 (2010).
27. M. Bernabei, A.J. Moreno, J. Colmenero, Phys. Rev. Lett. **101**, 255701 (2008).
28. M. Bernabei, A.J. Moreno, J. Colmenero, J. Chem. Phys. **131**, 204502 (2009).
29. M. Bernabei, A.J. Moreno, E. Zaccarelli, F. Sciortino, J. Colmenero, J. Chem. Phys. **134**, 024523 (2011).
30. W. Paul, D. Bedrov, G.D. Smith, Phys. Rev. E **74**, 021501 (2006).
31. J. Colmenero, A. Narros, F. Alvarez, A. Arbe, A.J. Moreno, J. Phys.: Condens. Matter **19**, 205127 (2007).
32. S. Capponi, A. Arbe, F. Alvarez, J. Colmenero, B. Frick, J.P. Embs, J. Chem. Phys. **131**, 204901 (2009).
33. Y. Khairy, F. Alvarez, A. Arbe, J. Colmenero, Phys. Rev. E **88**, 042302 (2013).
34. C. Bennemann, J. Baschnagel, W. Paul, Eur. Phys. J. B **10**, 323 (1999).
35. M. Aichele, J. Baschnagel, Eur. Phys. J. E **5**, 229 (2001).
36. T. Voigtmann, Europhys. Lett. **96**, 36006 (2011).
37. M. Rubinstein, R.H. Colby, *Polymer Physics* (Oxford University Press, Oxford, 2003).
38. M. Doi, S.F. Edwards, *The Theory of Polymer Dynamics* (Oxford University Press, Oxford, 1986).
39. B. Schnell, H. Meyer, C. Fond, J. Wittmer, J. Baschnagel, Eur. Phys. J. E **34**, 97 (2011).
40. L. Larini, A. Ottochian, C. De Michele, D. Leporini, Nat. Phys. **4**, 42 (2008).
41. A. Barbieri, D. Prevosto, M. Lucchesi, D. Leporini, J. Phys.: Condens. Matter **16**, 6609 (2004).
42. R.A.L. Vallée, W. Paul, K. Binder, J. Chem. Phys. **132**, 034901 (2010).
43. S. Peter, H. Meyer, J. Baschnagel, J. Polym. Sci. B **44**, 2951 (2006).
44. M. Solar, H. Meyer, C. Gauthier, C. Fond, O. Benzerara, R. Schirrer, J. Baschnagel, Phys. Rev. E **85**, 021808 (2012).
45. R. Everaers, S.K. Sukumaran, G.S. Grest, C. Svaneborg, A. Sivasubramanian, K. Kremer, Science **303**, 823 (2004).
46. S.C. Plimpton, Comput. Phys. **117**, 1 (1995).
47. R. Auhl, R. Everaers, G.S. Grest, K. Kremer, S.J. Plimpton, J. Chem. Phys. **119**, 12718 (2003).
48. W. Götze, J. Phys.: Condens. Matter **2**, 8485 (1990).
49. T.G. Fox, S. Loshaek, J. Polym. Sci. **15**, 371 (1955).
50. K.S. Schweizer, J.G. Curro, Adv. Chem. Phys. **98**, 1 (1997).
51. M. Aichele, S.H. Chong, J. Baschnagel, M. Fuchs, Phys. Rev. E **69**, 061801 (2004).
52. F. Weysser, A.M. Puertas, M. Fuchs, T. Voigtmann, Phys. Rev. E **82**, 011504 (2010).
53. J.P. Hansen, L. Verlet, Phys. Rev. **184**, 151 (1969).
54. M. Fuchs, K.S. Schweizer, J. Phys.: Condens. Matter **14**, R239 (2002).
55. J.P. Wittmer, A. Cavallo, H. Xu, J.E. Zabel, P. Polińska, N. Schulmann, H. Meyer, J. Farago, A. Johner, S.P. Obukhov *et al.*, J. Stat. Phys. **145**, 1017 (2011).
56. P.G. de Gennes, *Scaling Concepts in Polymer Physics* (Cornell University Press, Ithaca, 1996).
57. S. Krushev, W. Paul, Phys. Rev. E **67**, 021806 (2003).
58. W. Kob, H.C. Andersen, Phys. Rev. E **51**, 4626 (1995).
59. T. Gleim, W. Kob, Eur. Phys. J. B **13**, 83 (2000).
60. T. Voigtmann, A.M. Puertas, M. Fuchs, Phys. Rev. E **70**, 061506 (2004).
61. F. Weysser, D. Hajnal, Phys. Rev. E **83**, 041503 (2011).
62. J. Horbach, W. Kob, J. Phys.: Condens. Matter **14**, 9237 (2002).
63. J. Horbach, W. Kob, Phys. Rev. E **64**, 041503 (2001).
64. E. Flenner, G. Szamel, Phys. Rev. E **72**, 031508 (2005).
65. G. Foffi, W. Götze, F. Sciortino, P. Tartaglia, T. Voigtmann, Phys. Rev. E **69**, 011505 (2004).
66. X.C. Zeng, D. Kivelson, G. Tarjus, Phys. Rev. E **50**, 1711 (1994).
67. H.Z. Cummins, G. Li, Phys. Rev. E **50**, 1720 (1994).
68. S. Frey, PhD thesis, Université de Strasbourg, Strasbourg (2012) available from `http://www.sudoc.fr/165862653`.
69. T. Gleim, W. Kob, K. Binder, Phys. Rev. Lett. **81**, 4404 (1998).
70. L. Berthier, W. Kob, J. Phys.: Condens. Matter **19**, 205130 (2007).
71. F. Sciortino, L. Fabbian, S.H. Chen, P. Tartaglia, Phys. Rev. E **56**, 5397 (1997).
72. S.H. Chong, F. Sciortino, Phys. Rev. E **69**, 051202 (2004).
73. W. Kob, H.C. Andersen, Phys. Rev. E **52**, 4134 (1995).
74. M. Nauroth, W. Kob, Phys. Rev. E **55**, 657 (1997).
75. L. Berthier, G. Tarjus, Phys. Rev. E **82**, 031502 (2010).
76. S. Mossa, R. Di Leonardo, G. Ruocco, M. Sampoli, Phys. Rev. E **62**, 612 (2000).
77. A.E. Likhtman, *Polymer Science: A Comprehensive Reference*, Vol. **1** (Elsevier, Amsterdam, 2012) chapt. *Viscoelasticity and Molecular Rheology*, pp. 133–179.
78. J. Farago, A.N. Semenov, H. Meyer, J.P. Wittmer, A. Johner, J. Baschnagel, Phys. Rev. E **85**, 051806 (2012).
79. J. Farago, H. Meyer, J. Baschnagel, A.N. Semenov, Phys. Rev. E **85**, 051807 (2012).
80. T.G. Fox, P.J. Flory, J. Polym. Sci. **14**, 315 (1954).
81. G.B. McKenna, in *Comprehensive Polymer Science*, edited by C. Booth, C. Price, Vol. **2** (Pergamon, New York, 1986) pp. 311–362.
82. J. Hintermeyer, A. Herrmann, R. Kahlau, C. Goiceanu, E.A. Rössler, Macromolecules **41**, 9335 (2008).
83. A.L. Agapov, A.P. Sokolov, Macromolecules **42**, 2877 (2009).
84. J. Dudowicz, K.F. Freed, J.F. Douglas, Adv. Chem. Phys. **137**, 125 (2008).
85. M. Durand, H. Meyer, O. Benzerara, J. Baschnagel, O. Vitrac, J. Chem. Phys. **132**, 194902 (2010).
86. B. Lobe, J. Baschnagel, J. Chem. Phys. **101**, 1616 (1994).
87. T. Voigtmann, Phys. Rev. Lett. **101**, 095701 (2008).

88. N. Gnan, T.B. Schrøder, U.R. Pedersen, N.P. Bailey, J.C. Dyre, J. Chem. Phys. **131**, 234504 (2009).
89. D. Coslovich, C.M. Roland, J. Phys. Chem. B **112**, 1329 (2008).
90. C.M. Roland, S. Hensel-Bielowka, M. Paluch, R. Casalini, Rep. Prog. Phys. **68**, 1405 (2005).
91. L. Berthier, G. Tarjus, Eur. Phys. J. E **34**, 96 (2011).
92. J.P. Hansen, I.R. McDonald, *Theory of Simple Liquids* (Academic Press, London, 1986).
93. C. Bennemann, W. Paul, J. Baschnagel, K. Binder, J. Phys.: Condens. Matter **11**, 2179 (1999).
94. W. Götze, T. Voigtmann, Phys. Rev. E **61**, 4133 (2000).
95. F. Sciortino, P. Tartaglia, J. Phys.: Condens. Matter **11**, A261 (1999).
96. W. Paul, G.D. Smith, Rep. Prog. Phys. **67**, 1117 (2004).
97. F. Sciortino, W. Kob, Phys. Rev. Lett. **86**, 648 (2001).
98. A. Rinaldi, F. Sciortino, P. Tartaglia, Phys. Rev. E **63**, 061210 (2001).